

# High-Q Spectral Peaks and Nonstationarity in the Geomagnetic Field Over the 400-4000 $\mu\text{Hz}$ Band

Alan Chave (✉ [achave@whoi.edu](mailto:achave@whoi.edu))

Woods Hole Oceanographic Institution, Woods Hole <https://orcid.org/0000-0002-2460-1172>

David J Thomson

Queen's University

Douglas Luther

University of Hawai'i at Hilo

David Riegert

Queen's University

---

**Full paper**

**Keywords:** Geomagnetic field, solar normal mode

**Posted Date:** September 24th, 2020

**DOI:** <https://doi.org/10.21203/rs.3.rs-72827/v1>

**License:**   This work is licensed under a Creative Commons Attribution 4.0 International License.

[Read Full License](#)

---

1     **High-Q Spectral Peaks and Nonstationarity in the Geomagnetic Field over**  
2                                    **the 400-4000  $\mu$ Hz Band**

3

4     Alan D. Chave\*, Department of Applied Ocean Physics and Engineering,  
5             Woods Hole Oceanographic Institution, Woods Hole, MA 02543,  
6             USA; [achave@whoi.edu](mailto:achave@whoi.edu); ORCID: 0000-0002-2460-1172

7     David J. Thomson, Department of Mathematics and Statistics, Queen's  
8             University, Kingston, Ontario K7L 3N6, Canada; [djt@queensu.ca](mailto:djt@queensu.ca)

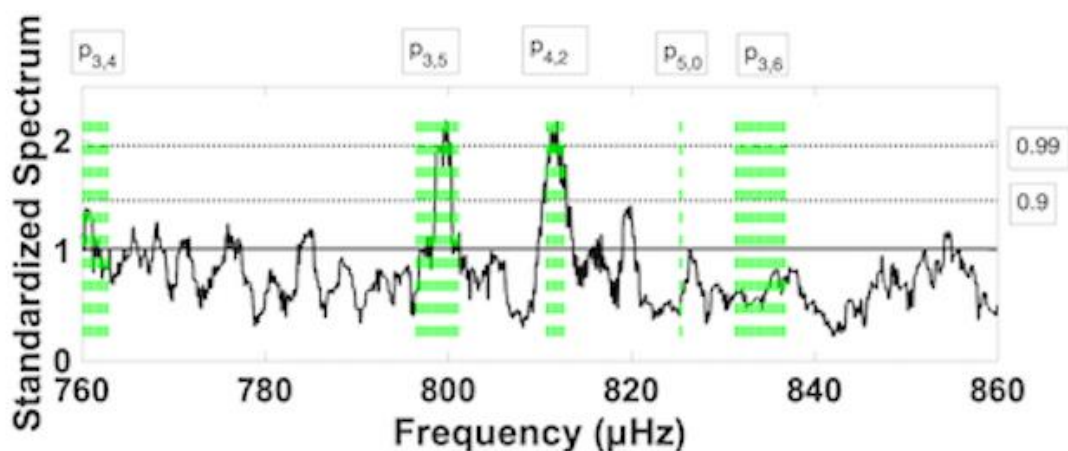
9     Douglas S. Luther, Department of Oceanography, JIMAR & SOEST,  
10            University of Hawai'i at Mānoa, Honolulu, HI 96822, USA;  
11            [dluther@hawaii.edu](mailto:dluther@hawaii.edu); ORCID: 0000-0003-0913-8260

12    David L. Riegert, Department of Mathematics and Statistics, Queen's  
13            University, Kingston, Ontario K7L 3N6, Canada;  
14            [driegert@mast.queensu.ca](mailto:driegert@mast.queensu.ca)

15    \*Corresponding Author

16 **Abstract**

17 This paper analyzes three 60 d sections of geomagnetic data from Honolulu  
18 Observatory during 2001–2, showing the ubiquitous presence of  
19 narrowband, very statistically significant, high  $Q$  features in multitaper  
20 power spectra, along with pervasive nonstationarity as measured by the  
21 frequency offset coherence over 400–4000  $\mu\text{Hz}$  (or 2500–250 s period). This  
22 behavior is nearly identical in the H and Z components of the geomagnetic  
23 field, and more subdued in the much weaker D component. The peak  
24 frequencies correlate well with the optically–measured frequencies of solar  
25 p–modes, and the raw  $Q$ s are defined by the resolution bandwidths of the  
26 estimates, with values ranging from hundreds to thousands. Further,  
27 spectral peaks are consistently coherent across frequency due to  
28 nonstationarity, and frequently exhibit cyclostationarity at offset  
29 frequencies of  $\pm 0.5$  cycles per day. None of these characteristics are  
30 consistent with internal magnetospheric processes. A mixture  
31 central/noncentral chi square model was fit to raw spectral estimates in an  
32 attempt to model narrowband, high  $Q$ , quasi–deterministic modes  
33 embedded in a stochastic background. This model yielded noncentral  
34 fractions of 0.13 (1000–2000  $\mu\text{Hz}$ ), 0.24 (1500–2500  $\mu\text{Hz}$ ), 0.35 (2000–3000  
35  $\mu\text{Hz}$ ), 0.30 (2500–3500  $\mu\text{Hz}$ ) and 0.17 (3000–4000  $\mu\text{Hz}$ ). These values  
36 suggest that up to 35% of the power in the geomagnetic field in the  
37 1000–4000  $\mu\text{Hz}$  band averaged over 60 days is forced by solar p–modes.



39 **Keywords**

40

41 Geomagnetic field; solar normal mode

## 42 Introduction

43 Thomson et al. (1995, 2001) showed that the signatures of solar normal  
44 modes could be detected in both solar wind particle fluxes propagating out  
45 from Sun and the interplanetary magnetic field at distances of as much as  
46 5.5 AU from Sun. Thomson et al. (2007), and Thomson and Vernon (2015,  
47 2016), present comprehensive analyses of space and terrestrial data (e.g.  
48 seismic, geomagnetic, barometric and particle flux types), and demonstrate  
49 that spectra computed from them contain pervasive, narrowband, high  $Q$   
50 features whose frequencies and  $Q$ s are consistent with normal modes of Sun  
51 at frequencies above  $\sim 250$   $\mu$ Hz. Thomson et al. (2007) also showed high  
52 coherence of the vector magnetic field measured by the Advanced  
53 Compositional Explorer (ACE) located at the L1 Lagrange point with that  
54 measured by Ulysses located near Jupiter at solar mode frequencies.  
55 Thomson (2012) found high coherence between ACE and GOES-10  
56 magnetic field and particle flux data at solar mode frequencies. Thomson  
57 and Vernon (2015) documented high coherence between the ACE and  
58 GOES-10 magnetic fields and terrestrial magnetic and seismic data at solar  
59 mode frequencies. Chave et al. (2019) extend some of these analyses to the  
60 deep ocean pressure field.

61 The idea that discrete solar modes could be launched from Sun into the  
62 solar wind and propagate out for 5 AU contradicted both “common  
63 knowledge” and the 1D MHD simulations possible in the late 1990s (e.g.,

64 Roberts et al., 1996). However, 3D simulations by Ghosh et al. (2009)  
65 showed that discrete modes and turbulence could coexist in space plasmas.

66 The space physics community has also studied magnetic pulsations over  
67 the same range of frequencies, although the majority of their investigations  
68 are hour to day long, event-based rather than statistical, and hence  
69 conclusions are conditioned on selection criteria. McPherron (2005) provides  
70 a review of magnetic pulsations. Kepko et al. (2002), Kepko and Spence  
71 (2003) and Kessel (2008) argue for solar wind dynamic pressure at the bow  
72 shock and magnetopause directly driving pulsations in the Pc5 range  
73 ( $\sim 1700\text{--}6700\ \mu\text{Hz}$ ) that in turn modify the ionosphere, yielding magnetic  
74 field changes at Earth's surface. Viall et al. (2009) provide an 11 y statistical  
75 study, concluding that about half of pulsation variance is due to direct solar  
76 wind forcing, with the remainder due to internal magnetospheric processes.  
77 Consequently, there is a substantial body of evidence for the presence of  
78 solar forcing at the outer boundaries of Earth's geomagnetic system  
79 propagating into its interior, in turn appearing at Earth's surface.

80 This paper extends the work of Thomson et al. (2007), and Thomson and  
81 Vernon (2015), providing a more extensive evaluation of terrestrial  
82 geomagnetic field variability for the presence of solar normal mode  
83 signatures. It will be shown that narrowband, high statistical significance,  
84 high  $Q$  features consistent with solar normal modes are ubiquitous across  
85 the 400–4000  $\mu\text{Hz}$  band in geomagnetic variations. It will also be shown

86 that peaks occur at non-modal frequencies that are coherent with modal  
87 peaks due to pervasive nonstationarity at solar mode frequencies.

## 88 **Solar Normal Modes**

89 Some of the internal fluctuations of Sun can be modeled as normal modes  
90 that are represented using a spherical harmonic expansion defined by  
91 “quantum numbers”  $n$ ,  $l$  and  $m$ . The radial order  $n$  gives the number of zeros  
92 along lines extending from Sun’s center, while the degree  $l$  denotes the  
93 number of latitudinal nodal lines. The azimuthal order  $m$  is the number of  
94 longitudinal nodal lines, where  $-l \leq m \leq l$ , and exists due to spherical  
95 asymmetry caused by Sun’s rotation and magnetic field. Each normal mode  
96 is characterized by a frequency  $f$  and a quality factor  $Q$  that is defined to  
97 be the ratio of the center frequency of a spectral peak to its full bandwidth  
98 at half power.

99 Over the frequency range considered in this paper, the predominant family  
100 of normal modes is the pressure ( $p_{n,l,m}$ ) type. For a recent review of the study  
101 of these modes, or helioseismology, see Christensen-Dalsgaard (2002). The  
102 p-modes are solar acoustic standing waves in the frequency range from  $\sim 250$   
103  $\mu\text{Hz}$  to the acoustic cutoff at  $\sim 5100 \mu\text{Hz}$ , or periods of about an hour to a few  
104 minutes. Their asymptotic frequencies are described by

$$105 \quad v_{n,l,m} \approx mv_r + v_o \left[ \frac{(l+\frac{1}{2})}{2} + n + \alpha \right] \quad (1)$$

106 where the rotational splitting term  $v_r \approx 440 \text{ nHz}$ ,  $v_o \approx 135 \mu\text{Hz}$  and  $\alpha$  is

107 the turning point phase shift that depends weakly on frequency. From (1),  
108 p-mode occurrence becomes dense above  $\sim 2000$   $\mu\text{Hz}$ , yielding about 100  
109 modes per  $\mu\text{Hz}$  if all possible rotational splitting terms are present, and so it  
110 may become increasingly difficult to uniquely identify a given mode in  
111 spectra with rising frequency. P-modes are probably excited by turbulence  
112 in the solar convection zone (Moretti et al., 2001), and hence their  
113 amplitudes are random rather than deterministic. The optically-measured  
114 amplitudes of p-modes (which typically reflect solar surface velocity) are  
115 weak at low frequencies, but rise rapidly at around  $2000$   $\mu\text{Hz}$  and peak at  
116  $2800$ – $3400$   $\mu\text{Hz}$  before falling off toward higher frequencies  
117 (Christensen-Dalsgaard, 2002; Fig. 11). The  $Q$ s of p-modes are several  
118 thousand, and increase with frequency. Consequently, mode forcing evolves  
119 slowly with time and persists for a few months, so that the power spectrum  
120 of a measurement driven by them is a weak function of time. In addition,  
121 optical measurements have shown that modal frequencies can vary as a  
122 function of solar activity by  $\sim 1$   $\mu\text{Hz}$  from their nominal values (Chaplin et  
123 al., 2000). Finally, because Earth rotates, modes observed terrestrially may  
124 be cyclostationary (i.e., periodically correlated), being modulated at  $\pm 1$  cycle  
125 per day (cpd;  $\pm 11.57$   $\mu\text{Hz}$ ), and there is evidence for additional splitting at  
126  $\pm 0.5$  cpd ( $\pm 5.79$   $\mu\text{Hz}$ ) caused by a nonlinear oscillation between the  
127 atmosphere and ionosphere (Gu et al., 2013). Taken together, these  
128 properties suggest that spectra containing p-modes will have unusual

129 properties with a high level of spectral variability.

130 In addition to this natural variability, if data sections under analysis are  
131 sufficiently short that two or more modes, or a given mode with multiple  
132 rotational singlets, fall within the resolution bandwidth, spectral estimates  
133 will appear erratic. For example, if two modes or singlets having similar  
134 amplitudes and the same phase occur within a resolution bandwidth of each  
135 other, a single peak will occur at their average frequency. Conversely, if the  
136 two modes are out of phase, nothing will be observed. The outcome is high  
137 spectral variability. Further, because there are many modes, there is a high  
138 probability that, in a given data section, there will be frequencies where  
139 modes are in phase while others are out of phase. In addition, peak  
140 frequencies will vary randomly when comparing results from different data  
141 sections.

142 An important characteristic of p-mode production is that about 1/3 of a  
143 given area on Sun at a specific time, or of a given time at a specific location  
144 on Sun, exhibits modal activity (Stix, 2004). Viall et al. (2009) showed that for  
145 about half of solar wind data segments exhibiting a spectral peak, a  
146 statistically significant corresponding peak was present in magnetospheric  
147 data. Combining these observations, it is reasonable to expect a given mode  
148 to be observed on Earth about 1/6 of the time; this number is consistent with  
149 measured detection occurrences given by He and Thomson (2009).

150 P-modes have been observed optically for the past thirty years at

151 frequencies above 1000  $\mu\text{Hz}$ , but the data are less reliable below that point.  
 152 Results from the Michelson Doppler Imager (MDI) on the Solar and  
 153 Heliospheric Observatory (SOHO) satellite are used for reference in this  
 154 study at frequencies above 1000  $\mu\text{Hz}$ ; see Scherrer et al. (1995) for a  
 155 description of MDI and Rhodes et al. (1997) for initial results. At frequencies  
 156 below 1000  $\mu\text{Hz}$ , Provost et al. (2000) provide mode frequencies, many of  
 157 which are the result of model calculations.

## 158 **Methods**

### 159 **Nonstationary Spectral Analysis**

160 When a time sequence  $x_t$  is generated by a process that is the  
 161 superposition of random, infinitesimal harmonic oscillators (which is called  
 162 a harmonizable random process), it has a spectral representation (Cramér,  
 163 1940)

$$164 \quad x_t = \int_{-1/2}^{1/2} e^{i2\pi\xi t} dX(\xi) \quad (2)$$

165 where  $E[dX(f)] = 0$ ,  $E$  symbolizes the expected value and  $X(f)$  is an unobservable  
 166 increments process whose statistical properties are of interest. The increments are  
 167 orthogonal if the process is stationary, and for two distinct frequencies  $f_1$  and  $f_2$

$$168 \quad E[dX(f_1)dX^*(f_2)] = S(f_1)\delta(f_1 - f_2)df_1df_2 \quad (3)$$

169 where  $S(f)$  is the population power spectral density and  $\delta(x)$  is the Dirac function. A  
 170 key property of a stationary process is that the power spectral density at distinct  
 171 frequencies is uncorrelated.

172 The spectral representation has non-orthogonal increments if a process  
173 is nonstationary, and (3) is superseded by

$$174 \quad E[dX(f_1)dX^*(f_2)] = S_L(f_1, f_2)df_1df_2 \quad (4)$$

175 where  $S_L$  is the Loève spectrum (Loève, 1945, 1946; Hanssen et al., 2004).

176 The power spectral density at distinct frequencies is correlated when a  
177 process is nonstationary. Further, when a nonstationary system is forced at  
178 a given frequency, power will be redistributed to other, unforced frequencies,  
179 and the correlation of the spectrum between the two frequencies will be  
180 high. This type of power transfer cannot be modeled as a linear process, so  
181 that forced nonstationarity is intrinsically nonlinear.

## 182 **Frequency Offset Coherence**

183 The spectral analyses in this paper are based on the multitaper method  
184 introduced by Thomson (1982), and a high level summary is contained in  
185 Supporting Information for Chave et al. (2019), Text S1. The advantages of  
186 the multitaper method include 1) it is a small sample theory with sample  
187 size explicit, 2) its bias can be quantified, 3) its resolution bandwidth is  
188 well-defined, 4) its variance efficiency is high, 5) it is data adaptive,  
189 yielding a low bias result even where the spectrum is weak, and 6) for  
190 Gaussian data, it is approximately maximum likelihood (Stoica and Sundin,  
191 1999).

192 The Loève spectrum is represented by the offset magnitude squared  
193 coherence (hereafter simply called the offset coherence) defined in

194 Supporting Information for Chave et al. (2019) Text S1, equation S7. The  
195 offset coherence has two independent variables, the ordinary frequency  $f$   
196 and the offset frequency  $f'$ . For a stationary process, the offset coherence is  
197 zero except when  $f' = 0$ , where it is precisely one, but it may be nonzero at  
198 a different offset frequency for a nonstationary process. The statistics of the  
199 offset coherence are the same as for the ordinary coherence. In addition, a  
200 multitaper offset coherence has the resolution bandwidth on the ordinary  
201 frequency axis, but the Rayleigh resolution  $1/N\Delta$ , where  $N$  is the length of  
202 the time sequence and  $\Delta$  is the sample interval, on the offset frequency axis  
203 (Thomson, 2001). The latter quantity will hereafter be called a Rayleigh and  
204 denoted by  $\mathcal{R}$ .

205 Whether between time series or between frequencies within a single time  
206 series, the coherence is the generalized likelihood ratio test for  
207 independence (Schreier and Scharf, 2010; § 4.5.3). The offset coherence will  
208 be shown as a contour plot against ordinary and offset frequency.

209 Presentation of the offset coherence is carried out as in Thomson and  
210 Vernon (2015; § 9) and Chave et al. (2019, § 4.2) to emphasize the most  
211 coherent elements in the data. The offset coherence will be evaluated  
212 conditional on its true value being zero, implying no nonstationarity. The  
213 probability density function for coherence is given in Thomson and Chave  
214 (1991, Eq. 2.53; note that the factor  $m - 1$  at the beginning of that equation  
215 should be in the numerator), and when the true coherence is zero, reduces to

216 
$$p(\hat{\gamma}^2) = (K - 1)(1 - \hat{\gamma}^2)^{K-2} \quad (5)$$

217 where  $K$  is the number of Slepian sequences employed in the multitaper estimator.

218 Integrating (5) over 0 to  $x$ , where  $x \leq 1$ , yields the cumulative probability distribution  
219 (cdf)

220 
$$P(x) = 1 - (1 - x)^{K-1} \quad (6)$$

221 The offset coherence is plotted as

222 
$$-\log_{10}(1 - P) = -(K - 1) \log_{10}(1 - \hat{\gamma}^2) \quad (7)$$

223 clipped at a value of 4. Values of 1, 2, 3 and 4 for (7) correspond to the 0.9,  
224 0.99, 0.999 and  $\geq 0.9999$  probability levels that two frequencies are correlated.

## 225 **Data**

226 The data used in this study are standard one minute measurements of  
227 the north (H), east (D) and vertical (Z) magnetic fields from Honolulu  
228 Observatory located at 21.3166°N, 157.9996°W from 4/2001–5/2002. This  
229 data segment was chosen for consistency with prior analyses in Chave et al.  
230 (2019). The data contain frequent gaps of hours to a few d over the initial ~9  
231 months. The analysis of data for solar modes requires section lengths that  
232 are sufficiently long to provide adequate frequency resolution, but short on  
233 the time scale for nonstationary variability so that a given mode will be  
234 persistent. Thomson and Vernon (2015) and Chave et al. (2019) utilized 60 d  
235 sections as a compromise between these two issues. For a 60 d data section,  
236  $\mathcal{R} = 0.19 \mu\text{Hz}$ . However, only three continuous 60 d intervals are present in  
237 the geomagnetic record for year–days (relative to 1 Jan 2001) of 298–358,

238 358–418 and 424–484. These are centered in northern hemisphere mid–fall,  
239 mid–winter and mid–spring, respectively. Solar cycle 23 peaked in late  
240 2001, so the geomagnetic activity level in these data is moderate to high.

241 Data analyses are carried out on time series after high pass filtering by  
242 twice passing a three pole Butterworth filter with the 3 dB point at 46  $\mu\text{Hz}$   
243 forward and backward across them, precluding the introduction of phase  
244 shifts. The multitaper spectrum of a section of the high passed geomagnetic  
245 record was then computed. Geomagnetic spectra will be modeled as a  
246 broadband red spectrum on which are superimposed ephemeral,  
247 narrowband features. To separate these, the log spectrum versus log  
248 frequency over the 100–5000  $\mu\text{Hz}$  band is post–whitened by removing a  
249 quadratic polynomial to yield a standardized spectrum. Note that  
250 polynomial detrending in the log–log domain is equivalent to taking the  
251 ratio of the computed spectrum and ten to the polynomial that was fit in the  
252 linear–linear domain. The result over a selected analysis band is plotted as  
253 linear frequency against linear standardized spectrum. Linear scale spectra  
254 are used because they enable definition of the bandwidth of spectral  
255 features, and are easily assessed for significance. Further, narrowband  
256 components occur as rectangular peaks in multitaper spectra with the  
257 resolution bandwidth, whereas random peaks appear as triangular features  
258 with a base width that is twice the resolution bandwidth (Thomson and  
259 Haley, 2014).

## 260 Spectra and Offset Coherences

261 Figure 1 shows the multitaper power spectrum of the high passed (but  
262 not standardized) geomagnetic data using a log frequency vs log power scale  
263 for the three data sections covering 200–4000  $\mu\text{Hz}$ . Spectra for each 60 d  
264 long data section were computed using a time–bandwidth of 5 and 9 Slepian  
265 sequence tapers, and then averaged, so there are about 54 degrees of  
266 freedom per frequency and the resolution bandwidth is 1.9  $\mu\text{Hz}$ . The H  
267 component (blue) has a spectrum that is about a decade larger than the Z  
268 component (yellow) at low frequencies, and their spectra merge toward high  
269 frequencies. The D component (red) is two decades weaker than H and one  
270 decade weaker than Z at low frequencies, transitioning to a two order of  
271 magnitude difference at high frequencies. There is no suggestion of spectral  
272 flattening, indicating that the noise level is not approached at high  
273 frequencies in any of the components, including extending to the Nyquist  
274 frequency of 8333  $\mu\text{Hz}$  (not shown).

275 Thomson et al. (2001), Thomson and Vernon (2015) and Chave et al.  
276 (2019) fit a mixture central/noncentral chi square distribution to raw  
277 standardized spectral estimates in an attempt to model a narrowband, high  
278  $Q$ , quasi–deterministic component embedded in a stochastic background in  
279 interplanetary magnetic, seismic and seafloor pressure data. In this context,  
280 deterministic means a phenomenon whose bandwidth is smaller than or  
281 comparable to  $1/\mathcal{R}$  and whose phase remains substantially constant over the

282 analysis interval. The mixture model

$$283 \quad d(\varepsilon, \lambda) = \varepsilon \chi_{2K}^2(\lambda) + (1 - \varepsilon) \chi_{2K}^2(0) \quad (8)$$

284 where  $\chi_{2K}^2$  denotes the chi square probability density function with  $2K$   
285 degrees of freedom,  $K = 9$ ,  $\varepsilon$  is the noncentral fraction and  $\lambda$  is the  
286 noncentrality parameter, was fit to each 60 d Honolulu data block over a set  
287 of 1000  $\mu\text{Hz}$  wide, overlapping frequency bands using the maximum  
288 likelihood method implemented using a nonlinear multivariable  
289 programming solver. Figure 2 contains examples of the mixture chi square  
290 model fit for the 2000–3000  $\mu\text{Hz}$  band where the noncentral fraction is  
291 largest. The empirical distribution of a set of spectral estimates is obtained  
292 using a kernel density estimator, which is the sum of smoothing operators  
293 applied repetitively across the support, and is in effect a smoothed  
294 probability histogram (Chave, 2017; § 4.8.3). For the year–day 298–358 data  
295 block, the empirical distribution is bimodal and long tailed, and is not fit  
296 well by the mixture model; this observation extends to all other frequency  
297 bands for this data interval. The fit is good for the remaining two data  
298 blocks, although the empirical distributions are not fit precisely around the  
299 mode. The average noncentral fractions using only the year–day 358–418  
300 and 424–484 data blocks are 0.13 (1000–2000  $\mu\text{Hz}$ ), 0.24 (1500–2500  $\mu\text{Hz}$ ),  
301 0.35 (2000–3000  $\mu\text{Hz}$ ), 0.30 (2500–3500  $\mu\text{Hz}$ ) and 0.17 (3000–4000  $\mu\text{Hz}$ ).  
302 These values approximately track with the optical power spectrum for solar  
303 modes given in Christensen–Dalsgaard (2002; Fig. 11), and suggest that up

304 to 35% of the power in the geomagnetic field data averaged over 60 d and  
305 1000–4000  $\mu\text{Hz}$  is from a noncentral chi square component.

306 The remainder of this section will present a series of exemplar  
307 standardized power spectra and offset coherences for the Honolulu  
308 geomagnetic data. The number of potential exemplars is much larger than  
309 shown, commensurate with the observation that a given solar normal mode  
310 occurs about 1/6 of the time. Because there are three Cartesian components  
311 to geomagnetic variations, presenting all of them for each time interval and  
312 analysis band would result in a prohibitive number of figures. As a result,  
313 only the H component that typically has the strongest response will be  
314 shown in this paper, with the remainder contained in Supplementary  
315 Information.

316 The mean of the standardized spectrum is one if the noncentral fraction  $\varepsilon$   
317 is zero, rising above that value as  $\varepsilon$  increases, and is shown for reference in  
318 the figures. The significance level of spectral features will be measured by  
319 the p-quantiles obtained from (8) after replacing the chi square probability  
320 density functions with the corresponding inverse cumulative distributions.  
321 The noncentral fraction and noncentrality parameter are computed by  
322 minimizing (8) over 600  $\mu\text{Hz}$  bands centered on the analysis interval; this  
323 proved to be the minimum bandwidth that produced stable estimates. As  
324 with the mean, the significance level increases as  $\varepsilon$  rises. Using percentiles  
325 from the mixture distribution means that a higher significance level

326 provides evidence that the spectrum comes from the noncentral part of the  
327 model. Further, the emphasis throughout this section will be on peaks that  
328 have a significance level of 0.99 or more in an attempt to be conservative  
329 and avoid over-interpretation of spectral features.

330 Figure 3a contains the standardized spectrum for year-days 298–358  
331 over 760–860  $\mu\text{Hz}$ , along with the frequencies including rotational splitting  
332 for the p-mode families denoted at the top of the figure taken from Provost  
333 et al. (2000). While there is considerable variability in the spectrum, there is  
334 a suggestion of forcing at  $p_{3,6}$ , with the frequency of  $\sim 835$   $\mu\text{Hz}$  exhibiting a  
335 square peak with a significance level of nearly 0.999 having the resolution  
336 bandwidth. The raw (i.e., measured)  $Q$  of this peak is 439, and is limited by  
337 the resolution bandwidth, hence may be much higher. This feature appears  
338 on the wings of a much stronger 0.999999 peak at  $\sim 845$   $\mu\text{Hz}$  having about  
339 three times the resolution bandwidth. In addition, broadband (relative to  
340 the resolution bandwidth) variability that is above the 0.99 significance  
341 level is observed over 770–780  $\mu\text{Hz}$ .

342 Figure 3b shows the offset coherence corresponding to Figure 3a. There  
343 is very high coherence (at least 0.9999 probability) over  $\sim 830$ -860  $\mu\text{Hz}$ ,  
344 encompassing  $p_{3,6}$  and the two peaks to its right in the form of a trapezoidal  
345 block. The trapezoidal shape can be understood as follows: if frequency  $f_1$  is  
346 coherent with frequency  $f_2 > f_1$ , then the coherence will be high at a  
347 positive offset frequency  $f_2 - f_1$  at frequency  $f_1$ , and hence at a negative

348 offset frequency  $f_1 - f_2$  at frequency  $f_2$ . Each of the trapezoidal blocks  
349 along zero offset frequency has an internal structure suggesting that each of  
350 the peaks in Figure 3a comprises numerous narrowband components that  
351 are themselves coherent. For example, the right trapezoidal block around  
352 zero offset frequency is highly coherent over 830–837  $\mu\text{Hz}$ , 840–850  $\mu\text{Hz}$   
353 and 853–860  $\mu\text{Hz}$ , respectively, which correspond to regions where the  
354 spectrum is above the 0.99 significance level in Figure 3a. Trapezoidal  
355 blocks also occur at offset frequencies consistent with coherence between the  
356 peaks. There is substantial coherence over  $\sim 770\text{--}800$   $\mu\text{Hz}$ , and this band of  
357 frequencies is both internally coherent and coherent with the 830–860  $\mu\text{Hz}$   
358 feature. In fact, substantial coherence extends beyond the boundaries of  
359 Figure 3b, as seen in the upper right and lower left corners.

360 Supplementary Information Figures S1–S2 show standardized spectra  
361 and offset coherences for the D and Z components corresponding to Figure 3.  
362 The D component spectrum and offset coherence are quite subdued compared  
363 to that for the H component, and the significance level in Figure S1a exceeds  
364 the 0.99 level at only one frequency. The Z component spectrum in Figure S2  
365 is very similar in appearance to the H component, displaying a somewhat  
366 weaker standardized spectrum and offset coherence, and the peak at  $p_{3,6}$  is  
367 absent.

368 Figure 4 shows the standardized spectrum and offset coherence for the H  
369 component over year–days 358–418, which is the 60 d block immediately

370 adjoining that presented in Figure 3. The character of the standardized  
371 spectrum is quite different from that in Figure 3a, and approaches the 0.99  
372 significance level at only three frequencies. In particular, a rectangular peak  
373 occurs at the 834  $\mu\text{Hz}$  frequency of the  $p_{3,6}$  family of normal modes. The  
374 weak peaks immediately adjacent are at  $\pm 0.5$  cpd ( $\pm 5.79$   $\mu\text{Hz}$ ) relative to the  
375 larger one. The offset coherence is much weaker than in Figure 3b, although  
376 a pattern of wide range correlation centered at several of the peaks is easily  
377 discerned. In particular, the 834  $\mu\text{Hz}$  peak is both locally coherent and  
378 coherent with the large peak at  $\sim 850$   $\mu\text{Hz}$ , as well as several lower  
379 frequency peaks.

380       Supplementary Information Figures S3–S4 show the D and Z component  
381 standardized spectra and offset coherences corresponding to Figure 4. The D  
382 spectrum is slightly stronger (as measured by the significance level) than  
383 the H component in Figure 4a, but is dissimilar in appearance. The offset  
384 coherence is also stronger than in Figure 3b, especially between  $\sim 810$ – $835$   
385  $\mu\text{Hz}$  where it reaches the 0.9999 significance level. By contrast, the Z  
386 component spectrum and offset coherence closely match those for the H  
387 component, with slightly higher significance levels in the standardized  
388 spectrum.

389       Figure 5a shows the standardized spectrum of the H component over  
390 760–860  $\mu\text{Hz}$  for year–days 424–484, which is the 60 d block nearly  
391 adjoining that given in Figure 4. The two largest peaks at  $\sim 800$  and  $\sim 811.5$

392  $\mu\text{Hz}$  occur within the  $p_{3,5}$  and  $p_{4,2}$  families of p-modes, and are each above  
393 the 0.99 significance level. These peaks are also within 1 cpd (11.57  $\mu\text{Hz}$ ) of  
394 each other, suggesting possible cyclostationarity due to Earth's rotation. The  
395 full bandwidth at half power for the two peaks is 2 and 3  $\mu\text{Hz}$ , yielding raw  
396  $Q$ s of 400 and 270, respectively.

397 Figure 5b shows the offset coherence for the data section and frequency  
398 band of Figure 5a. Offset coherence is evident at zero offset frequency for  
399 the spectral peak at  $p_{4,2}$  (811.5  $\mu\text{Hz}$ ) that is in turn coherent with other  
400 frequencies above and below that point. However, offset coherence is weak  
401 at the 800  $\mu\text{Hz}$  peak.

402 Supplementary Information Figures S5–S6 present standardized spectra  
403 and offset coherences for the D and Z components corresponding to Figure 5.  
404 The D component standardized spectrum rarely exceeds the 0.9 significance  
405 level, and appears to largely be noise. The Z component spectrum and offset  
406 coherence are very similar to those for the H component, with a slightly  
407 stronger standardized spectrum but a weaker offset coherence.

408 Figure 6a shows the H component standardized spectrum over  
409 1310–1410  $\mu\text{Hz}$  for year–days 424–484. The vertical red dashed lines show  
410 the central ( $m = 0$ ) frequencies of selected medium degree ( $l < 150$ ) p-modes  
411 taken from MDI as labeled above the plot; if the splitting terms were also  
412 shown, the figure would be covered with a picket fence of red lines. The  
413 strongest feature is the 0.99999 significance peak at 1388  $\mu\text{Hz}$ , which is

414 within 1  $\mu\text{Hz}$  of the center of the  $p_{2,48}$  family of p-modes. This peak has the  
415 resolution bandwidth, hence a raw  $Q$  of 695. A 0.999 peak also occurs near  
416 the central frequency of the  $p_{2,47}$  mode family at 1374  $\mu\text{Hz}$ , and in weaker  
417 form at the  $p_{3,28}$  and  $p_{1,78}$  mode families. Other weaker peaks occur over  
418  $\sim 1340\text{--}1350$   $\mu\text{Hz}$ .

419 Figure 6b shows the offset coherence corresponding to Figure 6a. The  
420 most obvious feature is the trapezoidal coherent block extending from  
421 1340–1390  $\mu\text{Hz}$  that indicates that the spectral peaks in Figure 6a over that  
422 frequency range are mutually coherent. Overall, Figure 6b depicts strong  
423 nonstationarity extending over the entire 1310–1410  $\mu\text{Hz}$  band and beyond.

424 Supplementary Information Figures S7–S8 show the D and Z component  
425 standardized spectrum and offset coherences corresponding to Figure 6. The  
426 D spectrum contains numerous weak, narrowband peaks between  
427  $\sim 1325\text{--}1365$   $\mu\text{Hz}$  that are mutually coherent. The Z component spectrum  
428 and offset coherence are very similar to those for the H component.

429 Figure 7a presents the standardized spectrum for the H component for  
430 year-days 358–418 over a frequency range of 2275–2375  $\mu\text{Hz}$ . There are  
431 two peaks (2301 and 2344  $\mu\text{Hz}$ ) that are above the 0.99 significance level,  
432 and an additional one (2336  $\mu\text{Hz}$ ) that nearly achieves this probability. All  
433 but the 2344  $\mu\text{Hz}$  peak coincide with the central frequencies of medium  
434 degree p-modes. Each of the spectral peaks has a full bandwidth at half  
435 power of 1 to 1.5 times the resolution bandwidth of 1.9  $\mu\text{Hz}$ , yielding raw  $Q$ s

436 of about 770. None of the peaks lie within  $\pm 0.5$  or  $\pm 1$  cpd of each other.

437 Figure 7b shows the offset coherence corresponding to Figure 7a. The  
438 frequency block 2290–2325  $\mu\text{Hz}$  is highly, mutually coherent, especially  
439 around the largest peak at 2301  $\mu\text{Hz}$ . Curiously, there is little coherence at  
440 the 2344  $\mu\text{Hz}$  peak in Figure 7a.

441 Supplementary Information Figures S9–S10 present spectra and offset  
442 coherences for the D and Z components corresponding to Figure 7. The D  
443 component spectrum is weak and lacks much resemblance to that for the H  
444 component, and the offset coherence is effectively zero. The Z component  
445 spectrum and offset coherence are weaker but similar to those for the H  
446 component.

447 Figure 8a shows the standardized spectrum over year–day 358–418 for  
448 the interval 3220–3420  $\mu\text{Hz}$ . This analysis band is twice as wide as in the  
449 preceding figures. The entire frequency interval is characterized by the  
450 presence of frequent, large, narrow peaks. The largest ( $>0.99999$   
451 significance) peak is at 3253  $\mu\text{Hz}$ , followed by a  $>0.9999$  peak at 3405  $\mu\text{Hz}$   
452 and  $>0.999$  peaks at 3232, 3261, 3269 and 3290  $\mu\text{Hz}$ . Further, there are  
453 fourteen peaks at or above the 0.99 significance level across the 200  $\mu\text{Hz}$   
454 analysis band. The largest peaks have a full bandwidth at half power of  
455 about 1.5 times the resolution bandwidth of 1.9  $\mu\text{Hz}$ , yielding a raw  $Q$  of  
456  $\sim 1100$ . Further, many of the peaks coincide with the center frequencies of  
457 medium degree p–modes, although curiously the largest peak at 3253  $\mu\text{Hz}$

458 does not.

459 Figure 8b shows the offset coherence corresponding to Figure 8a. This  
460 plot is quite striking in that every spectral peak in Figure 8a is strongly  
461 coherent with every other peak, and that characteristic clearly extends to  
462 both higher and lower frequencies than are displayed.

463 Supplementary Information Figures S11–S12 present spectra and offset  
464 coherences for the D and Z components corresponding to Figure 8. The D  
465 component spectrum is much weaker than for the H component, and the  
466 offset coherence is nearly zero. The Z component spectrum and offset  
467 coherence are very similar, although weaker, compared to that for the H  
468 component.

## 469 **Discussion**

470 A common characteristic of spectra presented in this paper and in  
471 Supplementary Information is that the H and Z components have similar  
472 spectra and offset coherences, while the D component is both weaker and  
473 dissimilar. This is commensurate with Figure 1, where the H and Z spectra  
474 are more similar in magnitude, while the D component is weaker by one to  
475 two orders of magnitude. Note also that over the frequency range of  
476 2000–4000  $\mu\text{Hz}$  (base 10 logarithms of 3.3 to 3.6) in Figure 1, spectral  
477 variability is enhanced relative to lower frequencies for the H and Z  
478 components, but not for the D component. The spectral variability is due to  
479 the presence of a substantial noncentral fraction over this frequency range.

480 Figure 9 shows the Kp index over the full 180 d data window, with red  
481 vertical dashed lines delineating the three 60 d analysis intervals. The Kp  
482 index is a quasi-logarithmic, planetary measure of geomagnetic activity  
483 with a range of 0–9 that is computed at 3 h intervals, and serves as a proxy  
484 for geomagnetic activity. Kp values under 5 denote quiet to active times and  
485 values of 5 or more denote minor to extreme geomagnetic storm activity.  
486 Extreme storms ( $K_p = 9$ ) occur roughly four times per  $\sim 11$  y solar cycle, and  
487 so are rare events.

488 Figure 9 indicates that the first analysis interval covering year–days  
489 298–358 contains 3 major to nearly extreme storms, while the remaining  
490 two analysis intervals display only minor to moderate storm activity.  
491 Standardized spectra from year–days 298–358 display frequent, broadband,  
492 large amplitude peaks (e.g., Figure 3a) with commensurate broadband, high  
493 probability offset coherence (e.g., Figure 3b), while the year–day 358–418  
494 and 424–484 intervals typically display peaks with the resolution  
495 bandwidth (e.g., Figures 4a and 5a) that have more localized, high  
496 probability offset coherence (e.g., Figures 4b and 5b). Given the association  
497 with a higher Kp, it is likely that the broadband features seen in Figure 3a  
498 are due to solar wind induced, nonmodal magnetospheric processes that can  
499 obscure solar mode peaks, which are more apparent when the geomagnetic  
500 activity level is weaker.

501 Figures 3–5 also illustrate the temporal variability of the spectrum and

502 its correlation structure through three (nearly) adjoining 60 d blocks. The  
503 temporal variability of the nonmodal element is certainly much higher than  
504 for solar normal modes, as is seen in the brevity of the high Kp intervals in  
505 the first 60 d block in Figure 9. These show up in the 60 d spectra because  
506 they are orders of magnitude more energetic than the background spectrum.  
507 There are five mode families shown in Figures 3a, 4a and 5a. Of these,  $p_{3,6}$   
508 is possibly identifiable in Figure 3a,  $p_{3,6}$  and possibly  $p_{4,2}$  are identifiable in  
509 Figure 4a, and  $p_{4,2}$  and  $p_{3,5}$  are identifiable in Figure 5a. This is broadly  
510 commensurate with the argument that a given mode should be observed on  
511 Earth about 1/6 of the time, which pertains only when high solar activity  
512 does not produce broadband interference.

513       There is evidence for the quasi-two day mode at  $\pm 0.5$  cpd in these data,  
514 but not for  $\pm 1$  cpd cyclostationarity. This is most easily seen by averaging  
515 the offset coherence across the peaks in ordinary frequency to produce a plot  
516 of offset frequency against transformed coherence. Figure 10 shows this  
517 quantity for the  $\sim 811.5$   $\mu\text{Hz}$  peak in Figure 5. Recall that the offset  
518 coherence against offset frequency has the Rayleigh resolution of 190 nHz.  
519 The clipped peak at zero offset frequency has two sidelobes at  $\pm 482$  nHz that  
520 are consistent with the  $m = \pm 1$  splitting terms. The  $-5.785$   $\mu\text{Hz}$  quasi-two  
521 day peak is present, along with two adjacent peaks on either side of it.  
522 These occur at frequency intervals of 470 nHz on average, again consistent  
523 with rotational splitting. However, there is no significant coherence at  $\pm 1$

524 cpd, which suggests that the second peak at  $\sim 800$   $\mu\text{Hz}$  in Figure 5a is not  
525 due to cyclostationarity.

526 Figure 11 shows the offset frequency vs offset coherence for the 3390  $\mu\text{Hz}$   
527 0.999 probability peak in Figure 8. The clipped peak at zero offset frequency  
528 is surrounded by three peaks with transformed coherence of 2  
529 (corresponding to 0.99 probability or higher) spaced at about 500 nHz that  
530 appear to be the  $m = \pm 3$  splitting terms. The  $-0.5$  cpd peak is clearly  
531 observed surrounded again by three peaks with a similar spacing. The  $+0.5$   
532 cpd peak is also present, but is somewhat obscured by activity at a higher  
533 frequency of unknown origin. Plots like Figures 10–11 were produced for the  
534 largest peaks in Figures 3–8, with similar results.

535 It is often straightforward to uniquely identify solar normal modes at  
536 frequencies under  $\sim 1000$   $\mu\text{Hz}$  where the degree and order are small and the  
537 frequency density of modes is low enough that unique identification is  
538 possible. Two clean examples are seen in Figures 4a and 5a, where strong,  
539 high  $Q$  peaks coincide respectively with the  $p_{3,5}$ ,  $p_{3,6}$  and  $p_{4,2}$  families of  
540 modes over the 760–860  $\mu\text{Hz}$  analysis band for different 60 d intervals. The  
541 substantially different appearance of the spectra for the two data segments  
542 in these figures is representative of pervasive nonstationarity that is  
543 apparent in Figures 4b and 5b.

544 There is more ambiguity at higher frequencies due to the rising  
545 frequency density of modes. For example, Figure 6a shows the central

546 ( $m = 0$ ) frequencies of several p-modes in close association with spectral  
547 peaks over 1340–1375  $\mu\text{Hz}$  that are mutually coherent (Figure 6b), yielding  
548 multiple potential identifications. Figure 7b displays a coherent trapezoidal  
549 block extending from 2290–2310  $\mu\text{Hz}$  that correlates to three substantial  
550 peaks (Figure 7a) corresponding to the center frequencies of three p-mode  
551 families. Figure 8 yields a similar outcome.

552 Further, the narrowband features seen in the standardized spectra have  
553 raw  $Q$  values determined by those of the multitaper estimator, hence serve  
554 as a lower bound on the actual  $Q$ . The raw  $Q$  values lie in the range of  
555 hundreds to over a thousand, increasing with frequency. This argues  
556 strongly for an origin outside of the magnetosphere, as no internal process  
557 with such a high  $Q$  has been identified in the literature. Magnetospheric  
558 resonances do exist over 1000–5000  $\mu\text{Hz}$  that have been explained by cavity  
559 or waveguide effects, where transient perturbation by the magnetopause  
560 provides the power to drive them. For example, Samson et al. (1991) present  
561 numerous spectra of such events from which  $Q$  can be estimated, yielding  
562 typical values of  $\sim 2$ – $5$ . These types of phenomena have lifetimes of minutes  
563 to hours, and cannot explain the observed peaks in the standardized  
564 spectrum figures that persevere for two months, nor can they explain the  
565 high  $Q$ s that are observed.

566 While previous work has largely concentrated on low degree modes, it  
567 appears that medium degree ( $l \lesssim 150$ ) p-modes are present in geomagnetic

568 data, as witness Figures 6, 7 and 8. A back of the envelope calculation serves  
569 to explain their presence. The radius of Sun  $R_{\odot}$  is  $\sim 109$  times that of Earth  
570  $R_{\oplus}$ , so that at  $l = 100$ , the width of a latitudinal band for a  $p_{n,l}$  mode is equal  
571 to  $\sim 2R_{\oplus}$ , with larger values pertaining at smaller degrees. A region of high  
572 modal activity having this scale will subtend a substantial fraction of the  
573 bow shock and magnetopause at a distance of  $\sim 2.3 \times 10^4 R_{\oplus}$  from the solar  
574 surface. It is likely that larger degrees will have a weaker affect, but there  
575 appears to be the potential for excitation at substantial values of the degree.

576       However, there is little evidence for forcing by high  $m$  modes as the  
577 degree rises. For example, Figure 7a displays a peak at  $\sim 2302 \mu\text{Hz}$  that  
578 could be due to forcing by the  $p_{7,39}$  family of modes. Presuming that all of the  
579 rotational splitting terms for degree 39 were present, the peak width would  
580 be  $\sim 35 \mu\text{Hz}$ , which is clearly not observed. In fact, the  $2302 \mu\text{Hz}$  peak is  
581 about twice the resolution bandwidth at half power, which would at most  
582 support the presence of  $m = \pm 5$ . This argument becomes even stronger at  
583 higher frequencies (Figure 8), where  $p$ -mode forcing at degree above 80 is  
584 typical. It is also supported by the offset frequency vs transformed coherence  
585 in Figures 10–11, where only low  $m$  splitting terms are observed.

586       Whether the forcing is broadband and transient, or modal and more  
587 slowly varying with time, the geomagnetic spectrum over  $400\text{--}4000 \mu\text{Hz}$  is  
588 pervasively and strongly nonstationary, as seen through the  $p = 0.99$  to  
589  $0.9999$  offset coherences in Figures 3b, 4b, 5b, 6b, 7b and 8b, and in the

590 corresponding Supplementary Information figures. The nonstationarity is  
591 both short and long range in frequency space. Short range nonstationarity is  
592 evident as trapezoidal offset coherence patches at distinct spectral peaks  
593 with bandwidths of order the resolution value throughout the figures. There  
594 is often internal structure to the peaks that is suggestive of interference  
595 between rotational singlets. Long range nonstationarity is witnessed as  
596 strong offset coherence patches at large values of the offset frequency. This  
597 is especially clear in Figure 8b, where features across the 200  $\mu\text{Hz}$  analysis  
598 band are highly coherent, which coherence extends beyond the  $\pm 100 \mu\text{Hz}$   
599 offset frequencies that are shown.

600 Thomson et al. (2007) proposed a conceptual model for the interplanetary  
601 magnetic field upstream of the bow shock consisting of “signal” comprising  
602 low attenuation plasma modes, “interference” consisting of a combination of  
603 attenuated plasma modes and the bulk flow of the solar wind, and “noise”  
604 comprised of solar flare detritus, coronal mass ejections and so on. Because  
605 propagation velocities are variable, interference can be constructive or  
606 destructive at random. When this mixture encounters Earth’s bow shock,  
607 solar modal signals will be coherent across the structure, while the noise is  
608 small scale. Consequently, the modal signals are amplified by the bow shock  
609 and magnetopause. Modal peaks in power spectra are progressively larger  
610 from ACE to GOES-10 to terrestrial magnetometers, with cyclostationarity  
611 observed in only the latter two data types. The modes couple to the

612 geomagnetic field and then into the solid earth to produce weak but  
613 detectable seismic signals. Thomson and Vernon (2015) present more  
614 detailed torque and energy arguments.

615       However, this mechanism does not address how the modes couple from  
616 Sun into the solar wind. The magnetic field above Sun from a solar mode is  
617 proportional to an integral of the velocity along a given mode rather than  
618 just the surface velocity that is measured optically. Modal magnetic  
619 signatures may be imposed on the magnetic environment around Sun, and  
620 hence into the solar wind, which does not require direct coupling of pressure  
621 modes from Sun into the solar wind. This is analogous to internal waves in  
622 the ocean, where surface measurements have not proven useful due to very  
623 weak surface displacements and/or velocities. However, in the 1970-80s,  
624 there was interest in modeling and successfully measuring the magnetic  
625 fields from internal waves above the ocean (e.g., Podney and Sager 1979;  
626 Peterson and Poehls 1982), with the primary focus on naval applications.

## 627 **Conclusions**

628       This paper has analyzed three 60 d sections of data from Honolulu  
629 Observatory during 2001–2, showing the ubiquitous presence of  
630 narrowband, high statistical significance, high  $Q$  features in multitaper  
631 power spectra and pervasive nonstationarity as measured by the frequency  
632 offset coherence over 400–4000  $\mu\text{Hz}$  (or 250–2500 s period). This behavior is  
633 nearly identical in the H and Z components of the geomagnetic field, and

634 more subdued in the much weaker D component. The peak frequencies  
635 correlate well with the optically-measured frequencies of solar p-modes,  
636 and the raw  $Q$ s are defined by the resolution bandwidth of the estimates  
637 (hence are lower bounds), with values ranging from 100s to 1000s. Further,  
638 spectral peaks are consistently coherent across frequency due to  
639 nonstationarity, and frequently exhibit cyclostationarity at offset  
640 frequencies of  $\pm 0.5$  cpd. None of these characteristics are consistent with  
641 internal magnetospheric processes, but rather are consistent with forcing by  
642 modal activity.

643 A mixture central/noncentral chi square model was fit to raw spectral  
644 estimates in an attempt to model narrowband, high  $Q$ , quasi-deterministic  
645 modes embedded in a stochastic background. This model failed for the  
646 initial 60 d interval due to high solar activity, and for the remaining data  
647 yielded noncentral fractions of 0.13 (1000–2000  $\mu$ Hz), 0.24 (1500–2500  
648  $\mu$ Hz), 0.35 (2000–3000  $\mu$ Hz), 0.30 (2500–3500  $\mu$ Hz) and 0.17 (3000–4000  
649  $\mu$ Hz). These values are in approximate agreement with the optical power  
650 spectrum for solar modes given in Christensen-Dalsgaard (2002), and  
651 suggest that up to 35% of the power in the geomagnetic field in the 1000-  
652 4000  $\mu$ Hz band averaged over 60 d is forced by solar modes. It also tracks  
653 with the seafloor pressure field as analyzed by Chave et al. (2019).

654 The initial 60 d analysis interval from late 2001 exhibits a  $K_p$  index of  
655 8–9 on several occasions. The spectrum across frequency during this

656 interval exhibits broadband (relative to the resolution bandwidth), high  
657 significance level (up to 0.999999) excursions that are broadly coherent  
658 across frequency, and are interpreted to be due to nonmodal forcing  
659 associated with high solar activity imposed on background modal forcing. By  
660 contrast, the spectra over the subsequent two 60 d intervals where  $K_p \lesssim 5$   
661 contain numerous narrowband, nonstationary features that are consistent  
662 with solar normal mode frequencies and  $Q_s$ .

663 Evidence is presented for the presence of medium spherical harmonic  
664 degree ( $l \lesssim 150$ ) p-modes at frequencies above  $\sim 1500 \mu\text{Hz}$ , although there is  
665 little indication for the presence of rotational splitting beyond small values  
666 of  $m$ . An argument is presented based on the size of the forcing area on Sun  
667 relative to the dimensions of the bow shock to explain this observation.

668 **Declarations**

669 **Ethics approval and consent to participate**

670 Not applicable.

671 **Consent for publication**

672 Not applicable.

673 **List of abbreviations**

674 ACE = Advanced Compositional Explorer

675 AU = astronomical unit, approximately the distance of Earth from Sun

676 cpd = cycle per day

677 d = day

678 GOES = Geostationary Operational Environmental Satellite

679 MDI = Michelson Doppler Imager instrument

680 P-mode = pressure mode

681  $Q$  = quality factor, defined to be the ratio of the center frequency of a

682 spectral peak to its full bandwidth at half power

683  $\mathcal{R}$  = Rayleigh, 1 over the time series length

684 SOHO = Solar and Heliospheric Observatory satellite

685 y = year

686 **Availability of data and materials**

687 The data used in this study are publicly available from Intermagnet at

688 <http://www.intermagnet.org/data-donnee/download-eng.php> - view. No

689 persistent URL for the exact data used here exists, and it is necessary to

690 select the observatory and time interval manually to download them.

### 691 **Competing interests**

692 The authors do not have any competing interests.

### 693 **Funding**

694 This work was supported at WHOI by the Walter A. and Hope Noyes Smith  
695 Chair for Excellence in Oceanography, at Queen's University by NSERC and  
696 at UH by NSF Grants OCE1460022 and OCE1948020.

### 697 **Authors' contributions**

698 ADC and DJT carried out the analyses reported in this paper. DSL and DLR  
699 reviewed the results and made suggestions for further work. ADC was  
700 responsible for manuscript preparation. All authors read and approved the  
701 final manuscript.

### 702 **Acknowledgements**

703 Not applicable.

### 704 **Authors' information**

705 ADC received a BS in physics from Harvey Mudd College and a PhD in  
706 oceanography from the Massachusetts Institute of Technology/Woods Hole  
707 Oceanographic Institution Joint Program in Oceanography. He then spent  
708 six years at Scripps Institution of Oceanography, one year as the J. Robert  
709 Oppenheimer Fellow at Los Alamos National Laboratory, and five years at  
710 AT&T Bell Laboratories before returning to Woods Hole, where he is a  
711 Senior Scientist. ADC is a Chartered Statistician and an elected Fellow of

712 the American Geophysical Union.

713 DJT received a BSc in mathematics and physics from Acadia University  
714 and became a Member of Technical Staff at Bell Telephone Laboratories in  
715 1965. He received MS (1967) and PhD (1971) degrees from Polytechnic  
716 Institute of Brooklyn. He played major roles in the WT4 Millimeter  
717 Waveguide and the first cellular phone system at Bell Labs before becoming  
718 a Distinguished Member of Technical Staff in the Communications Analysis  
719 Research Department. After retirement, he was appointed Canada Research  
720 Chair in Statistics and Signal Processing at Queen's University in 2002. He  
721 retired from Queen's University in 2018. DJT holds 25 patents, is a  
722 Chartered Statistician and a Professional Engineer in Ontario, and is an  
723 elected Fellow of the Institute of Electrical and Electronics Engineers and  
724 the Royal Society of Canada.

725 DSL received BS degrees in geophysics and electrical engineering from  
726 the Massachusetts Institute of Technology, and a PhD in oceanography from  
727 the Massachusetts Institute of Technology/Woods Hole Oceanographic  
728 Institution Joint Program. He was a Research Scientist for 12 years at  
729 Scripps Institution of Oceanography before being appointed Professor of  
730 Oceanography at the University of Hawai'i at Manoa. He is currently  
731 Director of the Joint Institute for Marine and Atmospheric Research.

732 DLR received a BS in mathematics and physics from the University of  
733 Alberta and an MS in mathematics from Queen's University. He is currently

734 a PhD candidate in the Department of Mathematics and Statistics at

735 Queen's University.

736 **Endnotes**

737 Not applicable.

738 **References**

- 739 Chaplin WJ, Appourchaux T, Elsworth Y, Isaak GR, Miller BA, New R  
740 (2000) Source of excitation of low- $l$  solar p modes: Characteristics and  
741 solar-cycle variations. *Mon. Not. R. Astr. Soc.* 314:75–86. doi:  
742 10.1046/j.1365-8711.2000.03335.x
- 743 Chave AD (2017) *Computational Statistics in the Earth Sciences*.  
744 Cambridge U. Press, Cambridge.
- 745 Chave AD, Luther DS, Thomson DJ (2019) High- $Q$  spectral peaks and  
746 nonstationarity in the deep ocean infragravity wave band: Tidal  
747 harmonics and solar normal modes. *J. Geophys. Res.* 124:2072–2087. doi:  
748 10.1029/2018JC014586
- 749 Christensen-Dalsgaard J (2002) Helioseismology. *Rev. Mod. Phys.*  
750 74:1073–1129. doi: 10.1103/RevModPhys.74.1073
- 751 Cramér H (1940) On the theory of stationary random processes. *Ann. Math.*  
752 41:215–230.
- 753 Ghosh S, Thomson DJ, Matthaeus W, Lanzerotti LJ (2009) Coexistence of  
754 turbulence and discrete modes in the solar wind. *J. Geophys. Res.*  
755 114:A08106. doi: 10.1029/2009JA014092
- 756 Gu S, Li T, Wang N, Riggins D, Fritts D (2013) Long-term observations of  
757 the quasi two-day wave by Hawaii MF radar. *J. Geophys. Res.*  
758 118:7886–7894. doi: 10.1002/2013JA018858
- 759 Hanssen A, Larsen Y, Scharf LL (2004) Complex time-frequency and  
760 dual-frequency spectra of harmonizable processes. *Proc. 12<sup>th</sup> Eur. Signal*  
761 *Proc. Conf.*, 1577–1580.
- 762 He H, Thomson DJ (2009) The canonical bicoherence: Part II—QPC test and  
763 its application in geomagnetic data. *IEEE Trans. Signal Proc.*  
764 57:1285–1292. doi: 10.1109/TSP.2009.2012603
- 765 Kepko L, Spence HE (2003) Observations of discrete, global magnetospheric  
766 oscillations driven by solar wind density variations. *J. Geophys. Res.* 108.

767 doi: 10.1029/2002JA009676.

768 Kepko L, Spence HE, Singer HJ (2002) ULF waves in the solar wind as  
769 direct drivers of magnetospheric pulsations. *Geophys. Res. Lett.* 29.  
770 doi:10.1029/2001GL014405.

771 Kessel RL (2008) Solar wind excitation of Pc5 fluctuations in the  
772 magnetosphere and on the ground. *J. Geophys. Res.* 113. doi:  
773 10.1029/2007JA012255.

774 Loève M (1945) Sur les fonctions aléatoires stationnaires de second ordre. *La*  
775 *Revue Scientifique* 83:297–303.

776 Loève M (1946) Fonctions aléatoires du second ordre. *La Revue Scientifique*  
777 84:195–206.

778 McPherron RL (2005) Magnetic pulsations: Their sources and relation to  
779 solar wind and geomagnetic activity. *Surv. Geophys.* 26:545-592. doi:  
780 10.1007/s10712-005-1758-7

781 Moretti PF, Cacciani A, Hanslmeier A, Messerotti M, Oliviero W, Ortuba W,  
782 Severino G, Warmuth A (2001) The source of solar oscillations:  
783 Convective or magnetic. *Astron. Astrophys.* 372:1038–1047.

784 Peterson, R.A., Poehls, K.A. (1982) Model spectrum of magnetic induction  
785 caused by ambient internal waves. *J. Geophys. Res.* 87:433-440.

786 Podney, W., Sager, R. (1979) Measurement of fluctuating magnetic gradients  
787 originating from oceanic internal waves. *Science* 205:1381-1382.

788 Provost J, Barthomieu G, Morel P (2000) Low-frequency p- and g-mode  
789 solar oscillations. *Astron. Astrophys.* 353:775–785.

790 Rhodes, EJ, Kosovichev AG, Schou, J, Scherrer, PH, Reiter, J (1997)  
791 Measurements of frequencies of solar oscillations from the MDI  
792 medium-l program. In Fleck, B, Švestka (eds) *The First Results from*  
793 *SOHO*. Springer, Dordrecht.

794 Roberts DA, Ogilvie K, Goldstein ML, Thomson DJ, MacLennan CG,  
795 Lanzerotti LJ (1996) The nature of the solar wind. *Nature* 381:31–32.

796 Samson JC, Greenwald RA, Ruohoniemi JM, Hughes TJ, Wallis DD (1991)  
797 Magnetometer and radar observations of MHD cavity modes in the  
798 Earth's magnetosphere. *Can. J. Phys.* 69:929–937.

799 Scherrer PH, Bogart RS, Bush RI, Hoeksema JT, Kosovichev AG, Scho J,  
800 Rosenberg W, Springer L, Tarbell TD, Title A, Wolfson CJ, Zayer I (1995)  
801 The solar oscillations investigation–Michelson Doppler Imager. In Fleck,  
802 B, Domingo, V, Poland, A (eds) *The Soho Mission*. Springer, Dordrecht.

803 Schreier PJ, Scharf LL (2010) *Statistical Signal Processing of*  
804 *Complex–Valued Data*. Cambridge U. Press., Cambridge.

805 Stix M (2004), *The Sun: An Introduction*, 2<sup>nd</sup> ed. Springer-Verlag, Berlin

806 Stoica P, Sundin T (1999) On nonparametric spectral estimation. *Circuits*  
807 *Syst. Signal Process* 18:169–181.

808 Thomson DJ (1982) Spectrum estimation and harmonic analysis. *Proc.*  
809 *IEEE* 70:1055–1096.

810 Thomson DJ (2001) Multitaper analysis of nonstationary and nonlinear  
811 time series data. In Fitzgerald W, Smith R, Walden A, Young P (eds)  
812 *Nonlinear and Nonstationary Signal Processing*. Cambridge U. Press,  
813 Cambridge.

814 Thomson DJ (2012) Background magnetospheric variability as inferred from  
815 long time series of GOES data. In Summers D, Mann IR, Baker DN,  
816 Schulz M (eds) *Dynamics of the Earth's Radiation Belts and Inner*  
817 *Magnetosphere*, Geophysical Monograph 199. Amer. Geophys. Union,  
818 Washington D.C.

819 Thomson DJ, Chave AD (1991) Jackknife error estimates for spectra,  
820 coherences, and transfer functions. In Haykin S. (ed) *Advances in*  
821 *Spectral Analysis and Array Processing*, Vol. 1. Prentice–Hall, Englewood  
822 Cliffs.

823 Thomson DJ, Haley CL (2014) Spacing and shape of random peaks in  
824 nonparametric spectrum estimates. *Proc. R. Soc. Lon.*, A470:20140101.  
825 doi: 10.1098/rspa.2014.0101

826 Thomson DJ, Vernon FL, III (2015) Unexpected, high-Q, low-frequency  
827 peaks in seismic spectra. *Geophys. J. Int.* 202:1690–1710. doi:  
828 10.1093/gji/ggv175

829 Thomson DJ, Vernon FL, III (2016) Some comments on the analysis of “big”  
830 scientific time series. *Proc. IEEE* 104:2220–2249.  
831 doi: 10.1109/JPROC.2016.2598218

832 Thomson DJ, Maclennan CG, Lanzerotti LJ (1995) Propagation of solar  
833 oscillations through the interplanetary medium. *Nature* 376:139–144.

834 Thomson DJ, Lanzerotti LJ, Maclennan CG (2001) The interplanetary  
835 magnetic field: Statistical properties and discrete modes. *J. Geophys.*  
836 *Res.* 106:15941–15962. doi: 10.1029/2000JA000113

837 Thomson DJ, Lanzerotti LJ, Vernon FL, III, Lessard MR, Smith LTP (2007)  
838 Solar modal structure of the engineering environment. *Proc. IEEE*  
839 95:1085–1132. doi: 10.1109/JPROC.2007.894712

840 Viall NM, Kepko L, Spence HE (2009) Relative occurrence rates and  
841 connection of discrete frequency in the solar wind density and dayside  
842 magnetosphere. *J. Geophys. Res.* 114:A01201. doi:  
843 10.1029/2008JA013334.

844 **Figure 1.** Multitaper power spectrum over 200–4000  $\mu\text{Hz}$  with a  
845 time-bandwidth of 5. The three 60 day long data sections enumerated in the  
846 text were separately processed using 9 Slepian tapers per estimate, and  
847 then averaged, yielding about 54 degrees of freedom per frequency. The  
848 three traces are H (blue), Z (yellow) and D (red).

849

850 **Figure 2.** The kernel density empirical distribution fit to standardized  
851 multitaper spectral estimates (solid line) along with the mixture model fit  
852 (dot-dash line), the central  $\chi^2$  component (dashed line) and the noncentral  
853  $\chi^2$  component (dotted line). From the top left and proceeding clockwise, the  
854 panels show the 2000–3000  $\mu\text{Hz}$  fit for year-days 298–358, 358–418 and  
855 424–484. The noncentral fractions for the latter two data blocks are 0.29  
856 and 0.40, respectively.

857

858 **Figure 3.** (a, bottom) H component standardized power spectral density  
859 versus frequency on linear scales over year–day 298–358 covering 760–860  
860  $\mu\text{Hz}$ . The time–bandwidth is 5 and there are 9 data tapers, yielding a  
861 resolution bandwidth of 1.9  $\mu\text{Hz}$  and 18 degrees of freedom per frequency.  
862 The solid horizontal line is the mean of the fitted mixture central/noncentral  
863 chi square distribution (8) over 400–1000  $\mu\text{Hz}$ , and the dashed horizontal  
864 lines are the 0.9 through 0.999999 quantiles of that distribution as labeled  
865 on the right. The green vertical dashed lines show the locations of solar  
866 p–modes including rotational splitting, as listed at the top. (b, top) Contours  
867 of the offset coherence transformed using (7) against frequency on the  
868 abscissa and offset frequency on the ordinate for the same frequency band  
869 and time interval as in (a). The time–bandwidth is 5 and 9 Slepian tapers  
870 were used, yielding 16 degrees of freedom per frequency. The color levels 1  
871 through 4 correspond to probability levels of 0.9 to 0.9999 that frequencies  
872 are correlated.

873

874 **Figure 4.** (a, bottom) H component standardized power spectral density  
875 versus frequency on linear scales over year–day 358–418 over 760–860  $\mu\text{Hz}$ .  
876 The time–bandwidth is 5 and there are 9 data tapers, yielding a resolution  
877 bandwidth of 1.9  $\mu\text{Hz}$  and 18 degrees of freedom per frequency. The solid  
878 horizontal line is the mean of the fitted mixture central/noncentral chi  
879 square distribution (8) over 400–1000  $\mu\text{Hz}$ , and the dashed horizontal lines  
880 are the 0.9 and 0.99 quantiles of that distribution as labeled on the right.  
881 The green vertical dashed lines show the locations of solar p–modes,  
882 including rotational splitting terms, as listed at the top. (b, top) Contours of  
883 the offset coherence transformed using (7) against frequency on the abscissa  
884 and offset frequency on the ordinate for the same frequency band and time  
885 interval as in (a). The time–bandwidth is 5 and 9 Slepian tapers were used,  
886 yielding 16 degrees of freedom per frequency. The color levels 1 through 4  
887 correspond to probability levels of 0.9 to 0.9999 that frequencies are  
888 correlated.

889

890 **Figure 5.** (a, bottom) H component standardized power spectral density  
891 versus frequency on linear scales over year–day 424–484 over 760–860  $\mu\text{Hz}$ .  
892 The time–bandwidth is 5 and there are 9 data tapers, yielding a resolution  
893 bandwidth of 1.9  $\mu\text{Hz}$  and 18 degrees of freedom per frequency. The solid  
894 horizontal line is the mean of the fitted mixture central/non-central chi  
895 square distribution (8) over 400–1000  $\mu\text{Hz}$ , and the dashed horizontal lines  
896 are the 0.9 and 0.99 quantiles of that distribution as labeled on the right.  
897 The green vertical dashed lines show the locations of solar p–modes,  
898 including rotational splitting terms, as listed at the top. (b, top) Contours of  
899 the offset coherence transformed using (7) against frequency on the abscissa  
900 and offset frequency on the ordinate for the same frequency band and time  
901 interval as in (a). The time–bandwidth is 5 and 9 Slepian tapers were used,  
902 yielding 16 degrees of freedom per frequency. The color levels 1 through 4  
903 correspond to probability levels of 0.9 to 0.9999 that frequencies are  
904 correlated.

905

906 **Figure 6.** (a, bottom) H component standardized power spectral density  
907 versus frequency on linear scales over year–day 424–484 over 1310–1410  
908  $\mu\text{Hz}$ . The time–bandwidth is 5 and there are 9 data tapers, yielding a  
909 resolution bandwidth of 1.9  $\mu\text{Hz}$  and 18 degrees of freedom per frequency.  
910 The solid horizontal line is the mean of the fitted mixture central/noncentral  
911 chi square distribution (8) over 1200–1800  $\mu\text{Hz}$ , and the dashed horizontal  
912 lines are the 0.9 through 0.99999 quantiles of that distribution as labeled on  
913 the right. The red dashed lines denote the center ( $m = 0$ ) frequencies of  
914 medium degree p–modes as labeled at the top. (b, top) Contours of the offset  
915 coherence transformed using (7) against frequency on the abscissa and  
916 offset frequency on the ordinate for the same frequency band and time  
917 interval as in (a). The time–bandwidth is 5 and 9 Slepian tapers were used,  
918 yielding 16 degrees of freedom per frequency. The color levels 1 through 4  
919 correspond to probability levels of 0.9 to 0.9999 that frequencies are  
920 correlated.

921

922 **Figure 7.** (a, bottom) H component standardized power spectral density

923 versus frequency on linear scales for year–day 358–418 over 2275–2375  
924  $\mu\text{Hz}$ . The time–bandwidth is 5 and there are 9 data tapers, yielding a  
925 resolution bandwidth of 1.9  $\mu\text{Hz}$  and 18 degrees of freedom per frequency.  
926 The solid horizontal line is the mean of the fitted mixture central/non-  
927 central chi square distribution (8) over 2000–2600  $\mu\text{Hz}$ , and the dashed  
928 horizontal lines are the 0.9 and 0.99 quantiles of that distribution as labeled  
929 on the right. The red dashed lines denote the center ( $m = 0$ ) frequencies of  
930 medium degree p–modes as labeled at the top. (b, top) Contours of the offset  
931 coherence transformed using (7) against frequency on the abscissa and  
932 offset frequency on the ordinate for the same frequency band and time  
933 interval as in (a). The time–bandwidth is 5 and 9 Slepian tapers were used,  
934 yielding 16 degrees of freedom per frequency. The color levels 1 through 4  
935 correspond to probability levels of 0.9 to 0.9999 that frequencies are  
936 correlated.

937

938 **Figure 8.** (a, bottom) H component standardized power spectral density  
939 versus frequency on linear scales for year–day 358–418 over 3220–3420  
940  $\mu\text{Hz}$ . The time–bandwidth is 5 and there are 9 data tapers, yielding a  
941 resolution bandwidth of 1.9  $\mu\text{Hz}$  and 18 degrees of freedom per frequency.  
942 The solid horizontal line is the mean of the fitted mixture central/non-  
943 central chi square distribution (8) over 3000–3600  $\mu\text{Hz}$ , and the dashed  
944 horizontal lines are the 0.9 through 0.99999 quantiles of that distribution as  
945 labeled on the right. The red dashed lines denote the center ( $m = 0$ )  
946 frequencies of medium degree p–modes as labeled at the top. (b, top)  
947 Contours of the offset coherence transformed using (7) against frequency on  
948 the abscissa and offset frequency on the ordinate for the same frequency  
949 band and time interval as in (a). The time–bandwidth is 5 and 9 Slepian  
950 tapers were used, yielding 16 degrees of freedom per frequency. The color  
951 levels 1 through 4 correspond to probability levels of 0.9 to 0.9999 that  
952 frequencies are correlated.

953

954 **Figure 9.** Kp index against time in 2001 year–days, with the vertical red  
955 dashed lines delineating the three 60 d time segments analyzed in this

956 paper. The hachured area between year–days 418 and 424 delineates a six  
957 day gap in the Honolulu Observatory data.

958

959 **Figure 10.** The offset coherence in Figure 5b averaged across the 811.5  $\mu\text{Hz}$   
960 peak in Figure 5a to give offset coherence against offset frequency. The  
961 vertical dashed lines show  $\pm 5.79$  and  $\pm 11.57$   $\mu\text{Hz}$  corresponding to the  $\pm 0.5$   
962 and  $\pm 1$  cpd cyclostationarity frequencies.

963

964 **Figure 11.** The offset coherence in Figure 8b averaged across the 3390  $\mu\text{Hz}$   
965 peak in Figure 8a to give offset coherence against offset frequency. The  
966 vertical dashed lines show  $\pm 5.79$  and  $\pm 11.57$   $\mu\text{Hz}$  corresponding to the  $\pm 0.5$   
967 and  $\pm 1$  cpd cyclostationarity frequencies.

# Figures

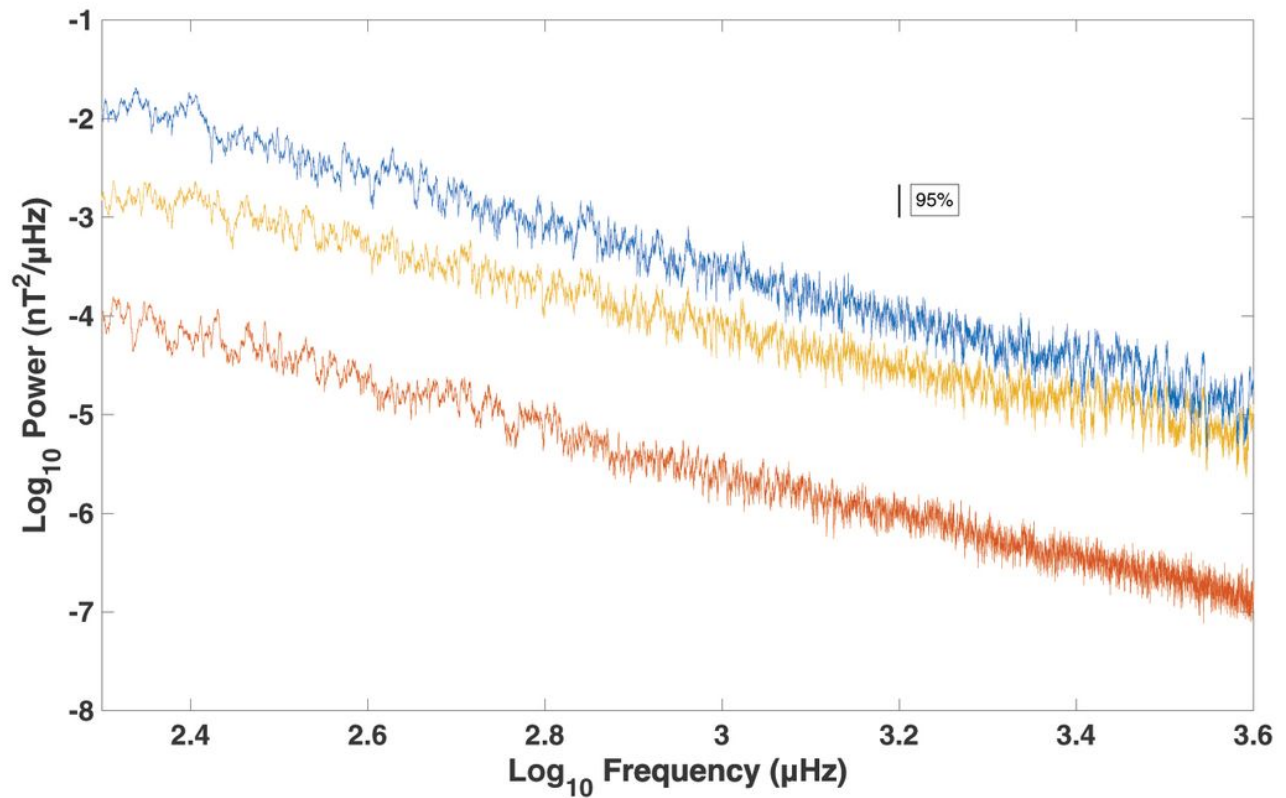
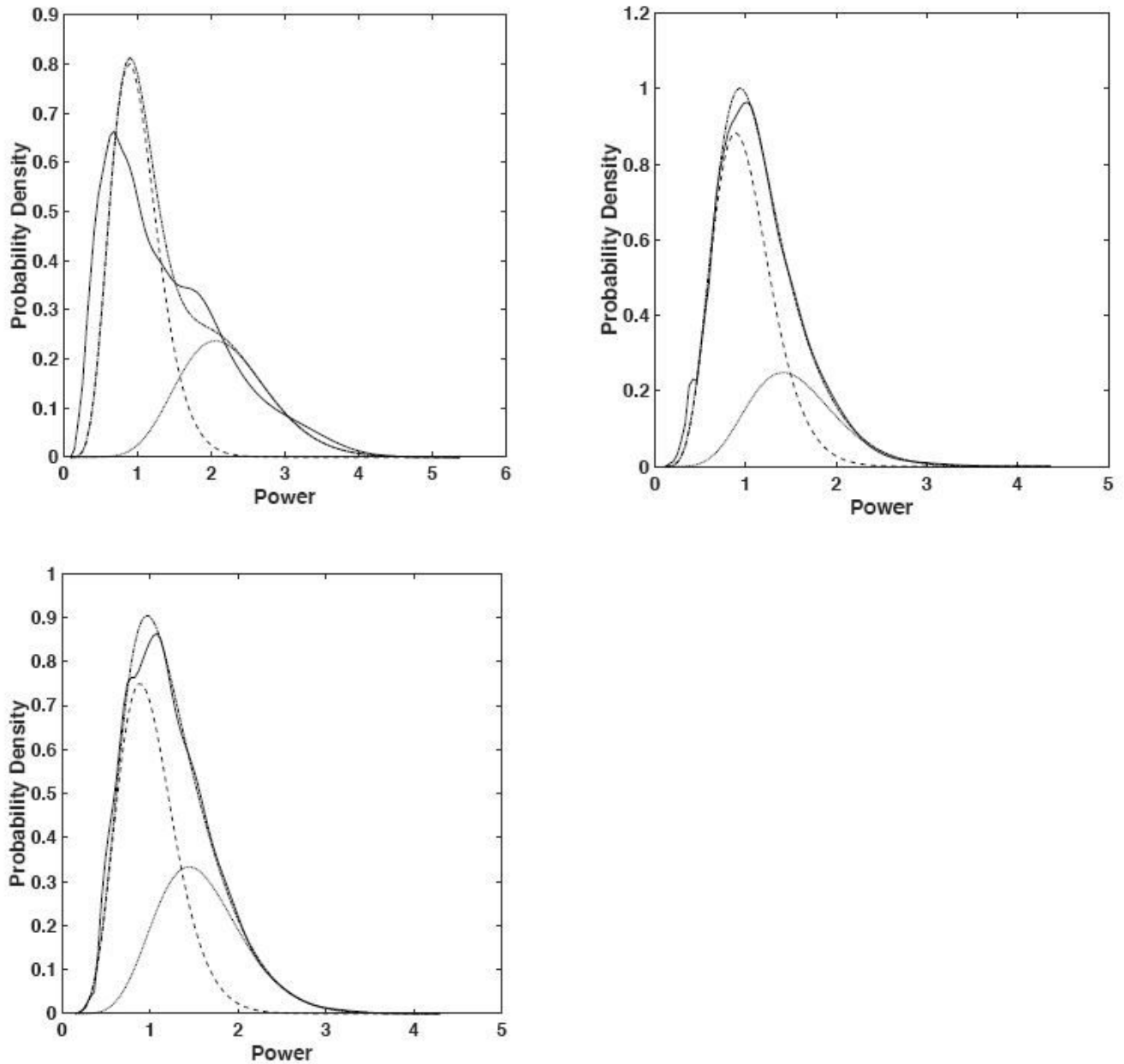


Figure 1

Multitaper power spectrum over 200–4000  $\mu\text{Hz}$  with a time–bandwidth of 5. The three 60 day long data sections enumerated in the text were separately processed using 9 Slepian tapers per estimate, and then averaged, yielding about 54 degrees of freedom per frequency. The three traces are H (blue), Z (yellow) and D (red).



**Figure 2**

The kernel density empirical distribution fit to standardized multitaper spectral estimates (solid line) along with the mixture model fit (dot-dash line), the central  $\chi^2$  component (dashed line) and the noncentral  $\chi^2$  component (dotted line). From the top left and proceeding clockwise, the panels show the 2000–3000  $\mu\text{Hz}$  fit for year-days 298–358, 358–418 and 424–484. The noncentral fractions for the latter two data blocks are 0.29 and 0.40, respectively.

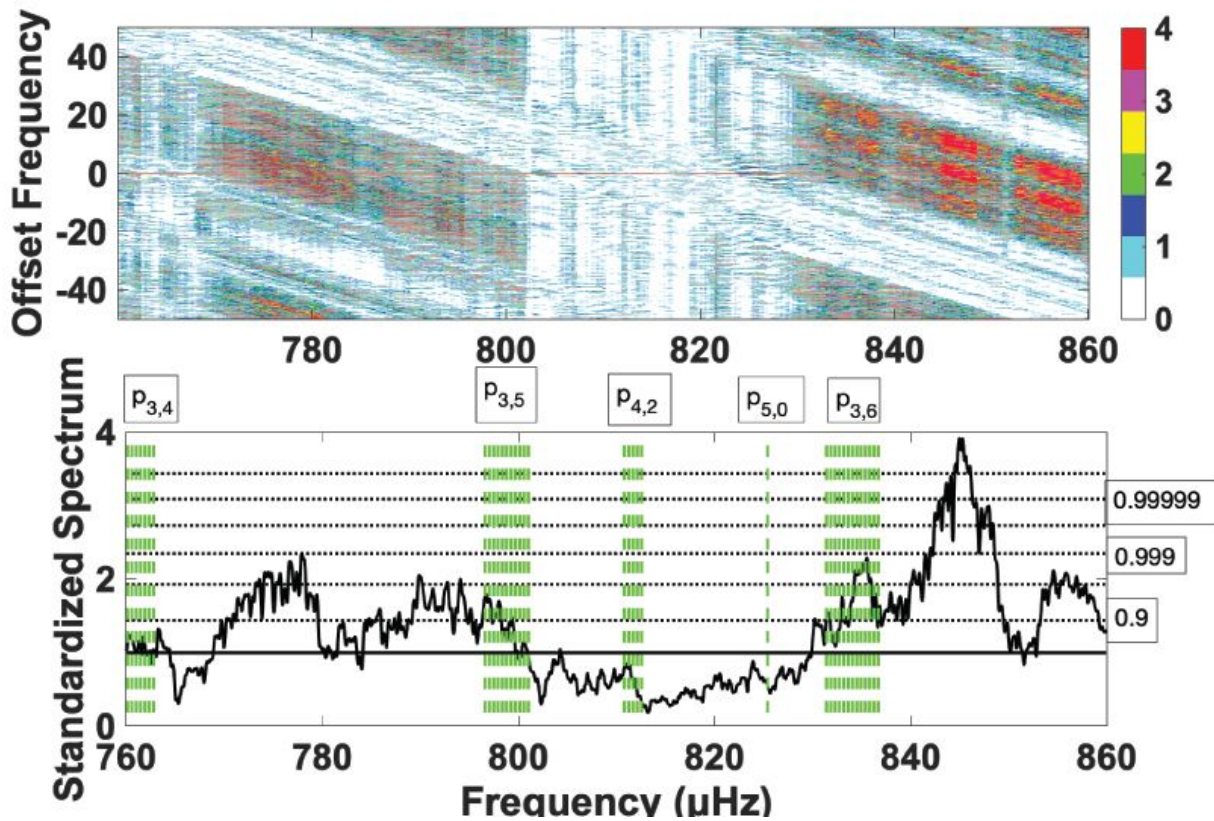


Figure 3

(a, bottom) H component standardized power spectral density versus frequency on linear scales over year-day 298–358 covering 760–860  $\mu\text{Hz}$ . The time-bandwidth is 5 and there are 9 data tapers, yielding a resolution bandwidth of 1.9  $\mu\text{Hz}$  and 18 degrees of freedom per frequency. The solid horizontal line is the mean of the fitted mixture central/noncentral chi square distribution (8) over 400–1000  $\mu\text{Hz}$ , and the dashed horizontal lines are the 0.9 through 0.999999 quantiles of that distribution as labeled on the right. The green vertical dashed lines show the locations of solar p-modes including rotational splitting, as listed at the top. (b, top) Contours of the offset coherence transformed using (7) against frequency on the abscissa and offset frequency on the ordinate for the same frequency band and time interval as in (a). The time-bandwidth is 5 and 9 Slepian tapers were used, yielding 16 degrees of freedom per frequency. The color levels 1 through 4 correspond to probability levels of 0.9 to 0.9999 that frequencies are correlated.

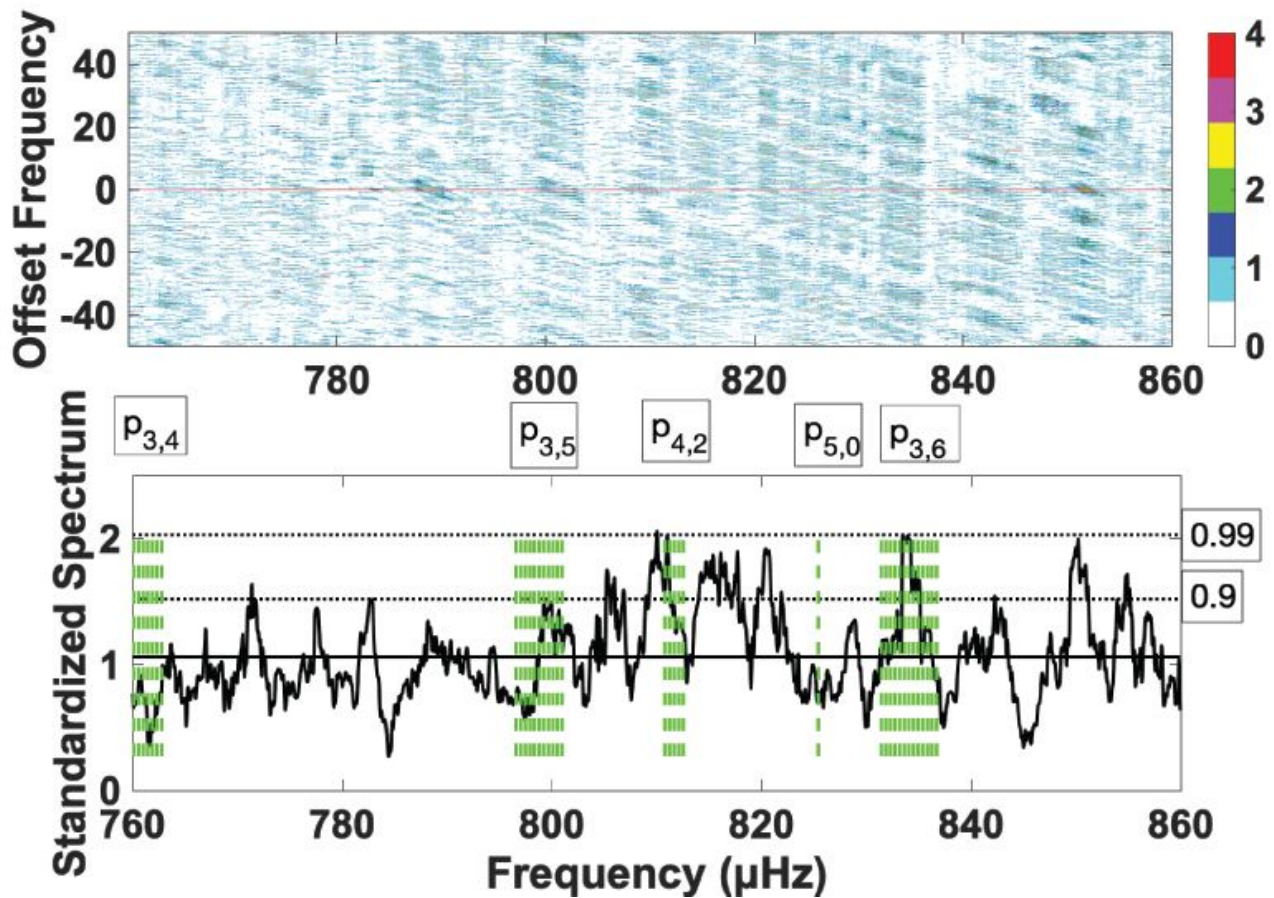


Figure 4

(a, bottom) H component standardized power spectral density versus frequency on linear scales over year-day 358–418 over 760–860  $\mu\text{Hz}$ . The time–bandwidth is 5 and there are 9 data tapers, yielding a resolution bandwidth of 1.9  $\mu\text{Hz}$  and 18 degrees of freedom per frequency. The solid horizontal line is the mean of the fitted mixture central/noncentral chi square distribution (8) over 400–1000  $\mu\text{Hz}$ , and the dashed horizontal lines are the 0.9 and 0.99 quantiles of that distribution as labeled on the right. The green vertical dashed lines show the locations of solar p-modes, including rotational splitting terms, as listed at the top. (b, top) Contours of the offset coherence transformed using (7) against frequency on the abscissa and offset frequency on the ordinate for the same frequency band and time interval as in (a). The time–bandwidth is 5 and 9 Slepian tapers were used, yielding 16 degrees of freedom per frequency. The color levels 1 through 4 correspond to probability levels of 0.9 to 0.9999 that frequencies are correlated.

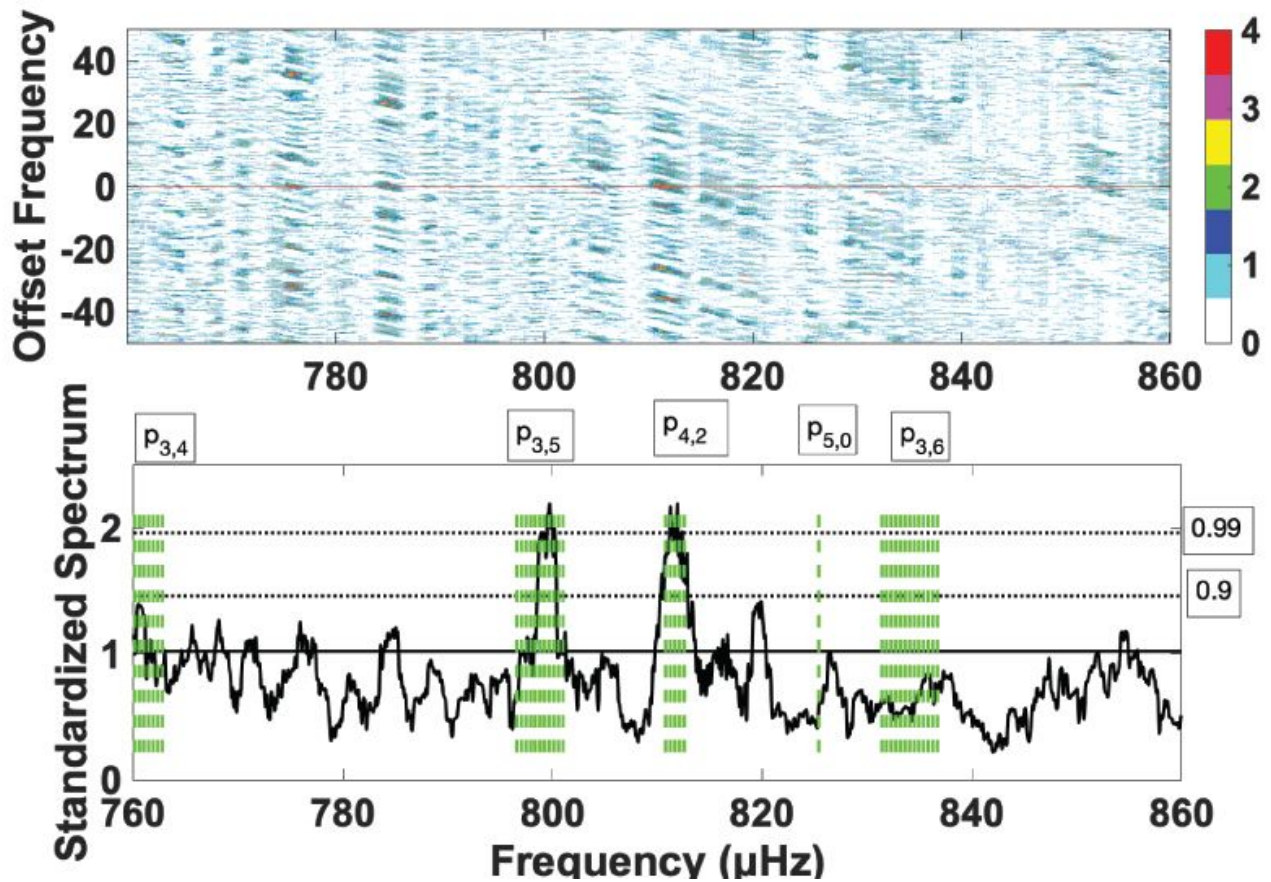


Figure 5

(a, bottom) H component standardized power spectral density versus frequency on linear scales over year-day 424–484 over 760–860  $\mu\text{Hz}$ . The time–bandwidth is 5 and there are 9 data tapers, yielding a resolution bandwidth of 1.9  $\mu\text{Hz}$  and 18 degrees of freedom per frequency. The solid horizontal line is the mean of the fitted mixture central/non-central chi square distribution (8) over 400–1000  $\mu\text{Hz}$ , and the dashed horizontal lines are the 0.9 and 0.99 quantiles of that distribution as labeled on the right. The green vertical dashed lines show the locations of solar p-modes, including rotational splitting terms, as listed at the top. (b, top) Contours of the offset coherence transformed using (7) against frequency on the abscissa and offset frequency on the ordinate for the same frequency band and time interval as in (a). The time–bandwidth is 5 and 9 Slepian tapers were used, yielding 16 degrees of freedom per frequency. The color levels 1 through 4 correspond to probability levels of 0.9 to 0.9999 that frequencies are correlated.

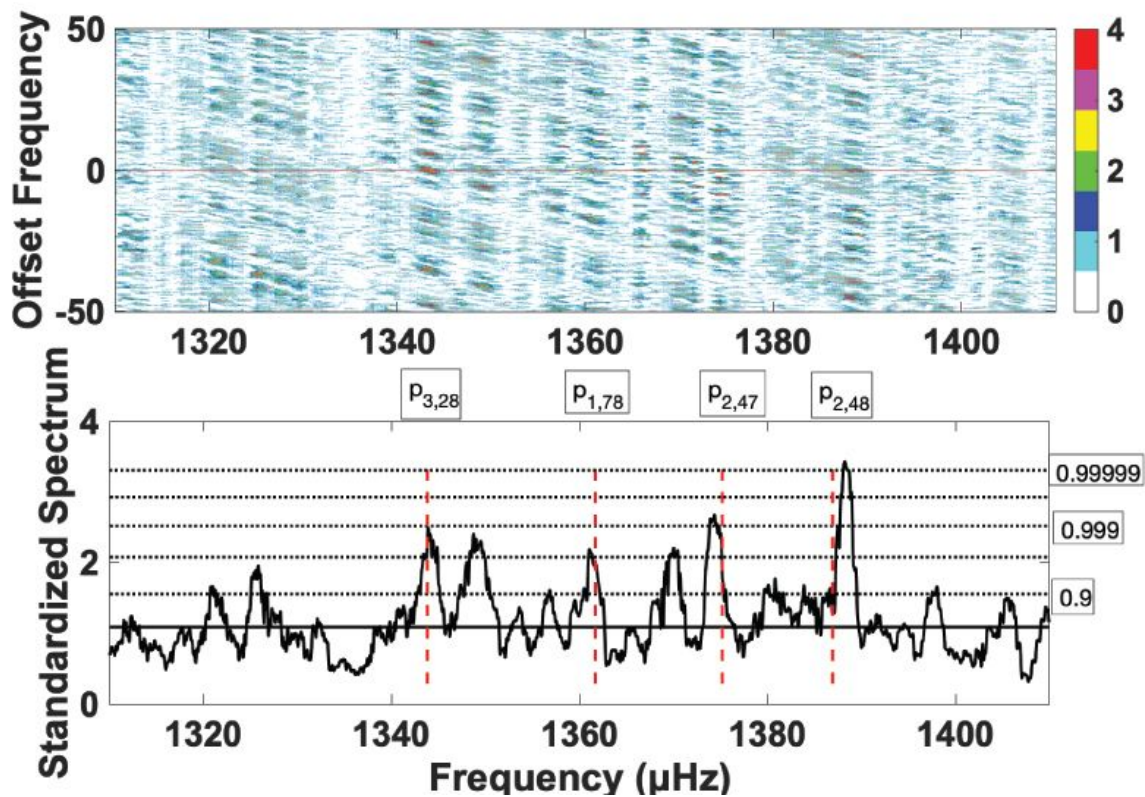


Figure 6

(a, bottom) H component standardized power spectral density versus frequency on linear scales over year-day 424–484 over 1310–1410  $\mu\text{Hz}$ . The time-bandwidth is 5 and there are 9 data tapers, yielding a resolution bandwidth of 1.9  $\mu\text{Hz}$  and 18 degrees of freedom per frequency. The solid horizontal line is the mean of the fitted mixture central/noncentral chi square distribution (8) over 1200–1800  $\mu\text{Hz}$ , and the dashed horizontal lines are the 0.9 through 0.99999 quantiles of that distribution as labeled on the right. The red dashed lines denote the center ( $m = 0$ ) frequencies of medium degree p-modes as labeled at the top. (b, top) Contours of the offset coherence transformed using (7) against frequency on the abscissa and offset frequency on the ordinate for the same frequency band and time interval as in (a). The time-bandwidth is 5 and 9 Slepian tapers were used, yielding 16 degrees of freedom per frequency. The color levels 1 through 4 correspond to probability levels of 0.9 to 0.9999 that frequencies are correlated.

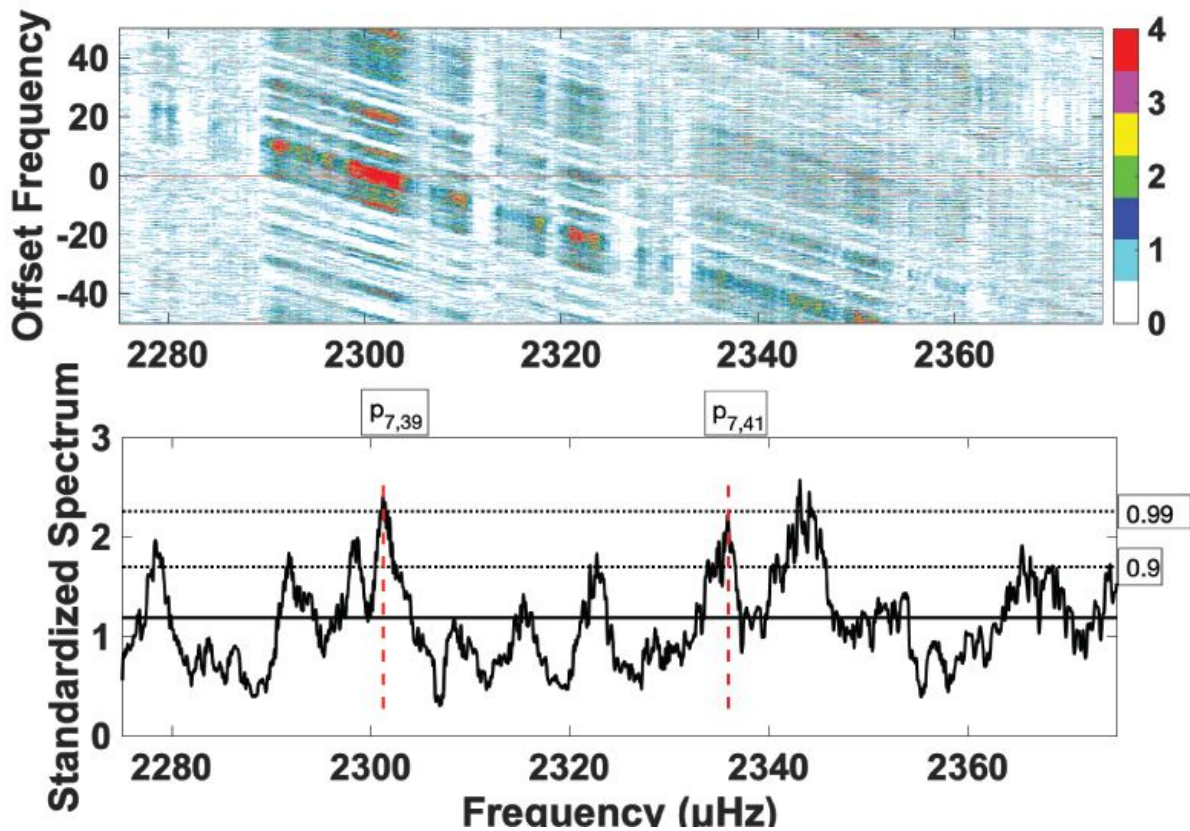


Figure 7

(a, bottom) H component standardized power spectral density versus frequency on linear scales for year-day 358–418 over 2275–2375  $\mu\text{Hz}$ . The time-bandwidth is 5 and there are 9 data tapers, yielding a resolution bandwidth of 1.9  $\mu\text{Hz}$  and 18 degrees of freedom per frequency. The solid horizontal line is the mean of the fitted mixture central/non-central chi square distribution (8) over 2000–2600  $\mu\text{Hz}$ , and the dashed horizontal lines are the 0.9 and 0.99 quantiles of that distribution as labeled on the right. The red dashed lines denote the center ( $m = 0$ ) frequencies of medium degree p-modes as labeled at the top. (b, top) Contours of the offset coherence transformed using (7) against frequency on the abscissa and offset frequency on the ordinate for the same frequency band and time interval as in (a). The time-bandwidth is 5 and 9 Slepian tapers were used, yielding 16 degrees of freedom per frequency. The color levels 1 through 4 correspond to probability levels of 0.9 to 0.9999 that frequencies are correlated.

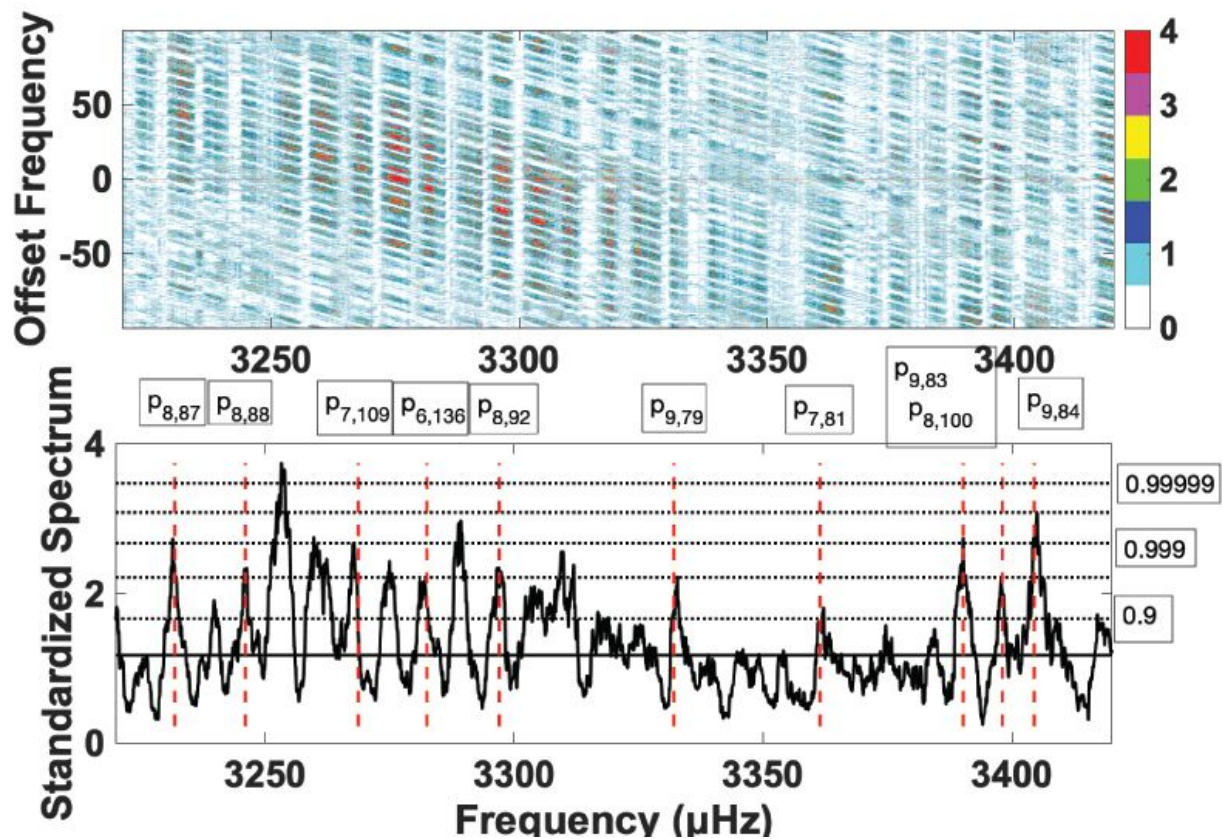


Figure 8

(a, bottom) H component standardized power spectral density versus frequency on linear scales for year-day 358–418 over 3220–3420  $\mu\text{Hz}$ . The time-bandwidth is 5 and there are 9 data tapers, yielding a resolution bandwidth of 1.9  $\mu\text{Hz}$  and 18 degrees of freedom per frequency. The solid horizontal line is the mean of the fitted mixture central/non-central chi square distribution (8) over 3000–3600  $\mu\text{Hz}$ , and the dashed horizontal lines are the 0.9 through 0.99999 quantiles of that distribution as labeled on the right. The red dashed lines denote the center ( $m = 0$ ) frequencies of medium degree p-modes as labeled at the top. (b, top) Contours of the offset coherence transformed using (7) against frequency on the abscissa and offset frequency on the ordinate for the same frequency band and time interval as in (a). The time-bandwidth is 5 and 9 Slepian tapers were used, yielding 16 degrees of freedom per frequency. The color levels 1 through 4 correspond to probability levels of 0.9 to 0.9999 that frequencies are correlated.

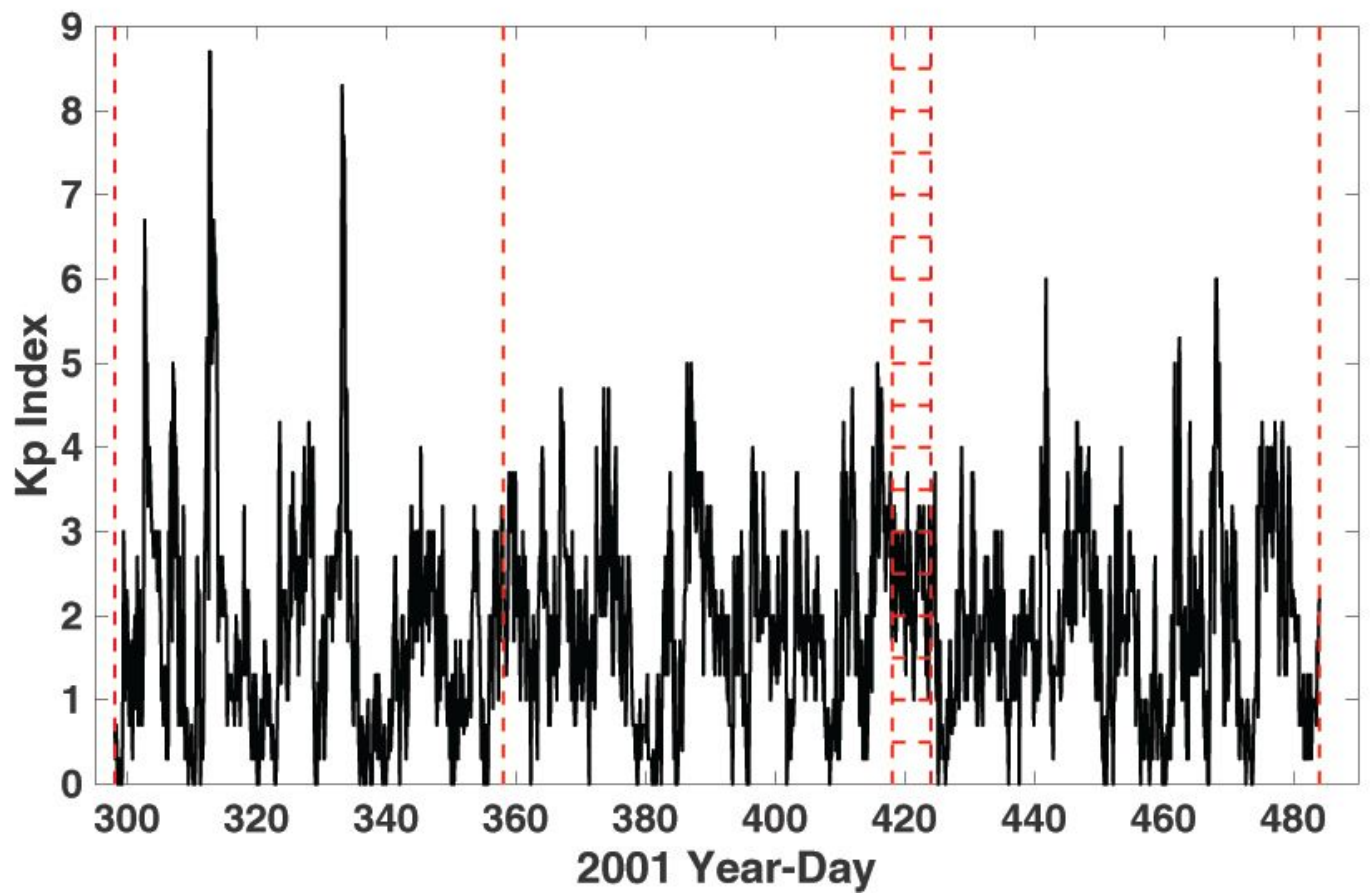
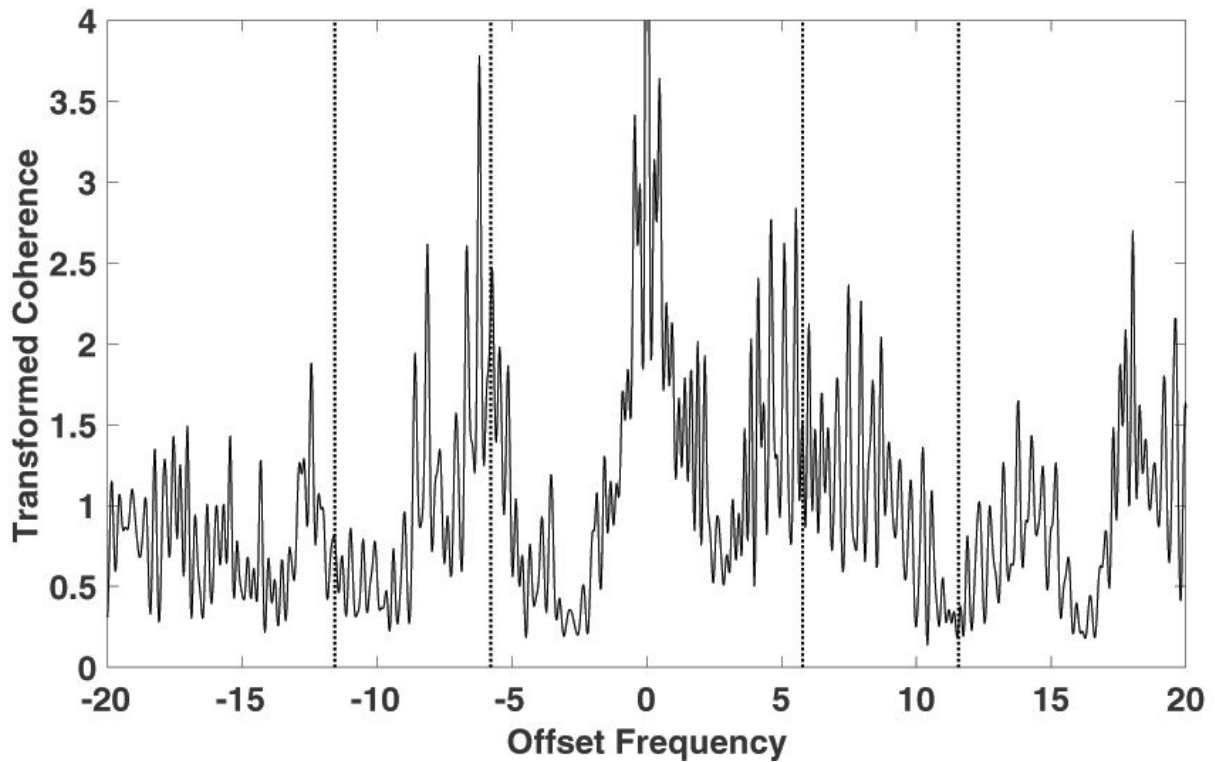


Figure 9

Kp index against time in 2001 year-days, with the vertical red dashed lines delineating the three 60 d time segments analyzed in this paper. The hachured area between year-days 418 and 424 delineates a six day gap in the Honolulu Observatory data.



**Figure 10**

The offset coherence in Figure 5b averaged across the 811.5  $\mu\text{Hz}$  peak in Figure 5a to give offset coherence against offset frequency. The vertical dashed lines show  $\pm 5.79$  and  $\pm 11.57$   $\mu\text{Hz}$  corresponding to the  $\pm 0.5$  and  $\pm 1$  cpd cyclostationarity frequencies.

Image not available with this version

**Figure 11**

The offset coherence in Figure 8b averaged across the 3390  $\mu\text{Hz}$  peak in Figure 8a to give offset coherence against offset frequency. The vertical dashed lines show  $\pm 5.79$  and  $\pm 11.57$   $\mu\text{Hz}$  corresponding to the  $\pm 0.5$  and  $\pm 1$  cpd cyclostationarity frequencies.

## Supplementary Files

This is a list of supplementary files associated with this preprint. Click to download.

- [graphicalabstract.png](#)
- [GeomagneticNonstationaritySupp.pdf](#)